Through-thickness crack growth resistance in fibre composites and its role in preventing ply cracking in cross-ply laminates

Wenkai Chang[a], L. R. Francis Rose[b], Shuying Wu[a, c], Anthony J. Kinloch[d], Chun H. Wang[a*]

[a] School of Mechanical and Manufacturing Engineering, University of New South Wales, Sydney, NSW 2052, Australia.

[b] Defence Science and Technology Group, Melbourne, VIC 3207, Australia.

[c] School of Engineering, Macquarie University, Sydney, NSW 2109, Australia.

[d] Department of Mechanical Engineering, Imperial College London, South Kensington Campus, London SW7 2AZ, U.K.

Abstract

A new mechanism is proposed to elucidate recent experimental observations of a transition from slow, stable through-thickness cracking to unstable growth in the 90° ply of a cross-ply laminate as the ply thickness increases above 40 µm for typical carbon fibre reinforced polymer composites. Herein we have identified that the transition is attributed to a rising crack-growth resistance (or R-curve) of transverse matrix cracks with increasing size. This new explanation is substantiated by obtaining the R-curve using a high-fidelity micromechanical model, followed by employing fracture mechanics principles to predict the progression and stability of through-thickness microcracking in a ply. The benefit of this new approach is that only one simulation is required to generate the R-curve, which can then be employed to predict the crack-growth behaviour for any ply thickness, instead of requiring separate simulations for each ply thickness, thereby reducing the computational burden considerably. This is particularly valuable for parametric studies to investigate the dependence on various material properties and computationally efficient analysis of large-scale structures. As illustrative examples, the dependence on matrix toughness and on volume fraction was investigated and simple linear relationships were identified for the steady-state value of crack-growth resistance. Such relationships can further reduce the computational burden, particularly when the relevant material properties may not be available from direct measurement, but can be reasonably estimated, as for cryogenic applications.

*Corresponding author: Chun-Hui Wang (E-mail: chun.h.wang@unsw.edu.au Tel: +61 2 93853232)

1. Introduction

Ply cracking, where transverse matrix cracks extend through the full thickness of a ply, is often the most critical initial failure mode in fibre composite laminates. This form of cracking is a major concern for composite vessels used for storing liquid or gaseous fuels, such as hydrogen and oxygen, because ply cracks can link up to form interconnected channels that cause fuel leaks and degrade the structural safety of the vessels. The pioneering work of Bailey and co-workers [1-3], as discussed in recent reviews [4, 5], identified two régimes for the thickness dependence of the ply cracking strain, or, equivalently, of the *in-situ* ply strength [6]. For "thin" plies, the ply cracking strain was found (experimentally and theoretically) to decrease with increasing the ply thickness, whereas for "thick" plies, the ply cracking strain is independent of the ply thickness. The transition from thin to thick régime was found to occur at a ply thickness of around 0.5 mm in cross-ply laminates, for both glass fibres (GFRP) and carbon fibres (CFRP).

Recent research on matrix cracking of thin-ply composites, however, has highlighted a gap in our understanding of the growth behaviour of through-thickness matrix cracks in plies of varying thickness. A through-thickness matrix crack is defined by the coalescence of at least two adjacent debondings between the fibre and matrix [7]. Slow and stable through-thickness matrix cracking was observed in laminate consisting of thin-plies of $40 \ \mu m$ in thickness, whereas unstable growth was found to occur in laminates with ply thickness of $80 \ \mu m$ or $160 \ \mu m$, as reported by Saito et al.[7]. These experimental observations have been closely reproduced in a high-fidelity micromechanical model by Arteiro et al. [8], whose work incorporates several recent developments in modelling of composites, relative to earlier micromechanical models [9-13], including an improved constitutive modelling for the matrix phase [14, 15]; see [16-20] for related recent work and reviews of multi-scale analysis of composites. These recent findings follow the development of tow-spreading technology, leading to commercially available ply thicknesses down to $15 \ \mu m$ [21, 22]. Ultra-thin plies offer benefits both because of the ability to use a larger number of ply orientations, thereby expanding the laminate design space for achieving an optimal lay-up, and because of improvements in mechanical properties, e.g. a 10% increase in the ultimate strength of quasi-isotropic CFRP laminates constructed from $40 \ \mu m$ plies [23], as well as improved notched tensile strength and fatigue resistance [21]. These benefits are of particular interest for cryogenic applications such as linerless propellant tanks for reusable launch vehicles and fuel storage for deep space explorations, where resistance to ply cracking due to residual thermal stresses, thermal-mechanical cycling, and associated anti-leakage properties are crucially required [24-26].

The stable through-thickness growth at very small ply thickness, transitioning to unstable growth with increasing ply (or layer) thickness as revealed by experimental observations and computational model

predictions are not accounted for by the currently available theoretical models that tend to focus on the tunnelling mode of a pre-existing full-thickness matrix crack [27-36], whose direction of growth is parallel to fibres. This lack of fundamental understanding of the mechanism of ply-thickness effect in thin- and ultra-thin ply laminates impedes improvement in laminate design for demanding applications such as linerless cryogenic fuel tanks.

The present work proposes a novel proposition to account for the experimental and computational results in [7, 8] in terms of an increasing crack-growth resistance for through-thickness matrix cracks. The principle is illustrated in Fig. 1. The implementation of this principle in the present work combines the micromechanical modelling approach of Arteiro et al. [8] with the embedded cell approach [11] to derive the required crack growth resistance curve (the R-curve) in a computationally efficient manner. Next, the crack-growth behaviour is predicted by applying linear elastic fracture mechanics (LEFM) [37, 38] to determine whether crack growth is stable or unstable; details are presented in Section 4. It is worth noting that this R-curve approach was not foreshadowed in previous micromechanical simulations [8-20], or theoretical models [27-36]. One advantage of the proposed crack-growth resistance approach is that it provides a computationally efficient method for determining the critical ply thickness for the transition from stable to unstable crack growth, because the R-curve can be generated, once and for all, from a single micromechanical model, instead of the several separate models that would be required for different ply thicknesses in a trial-and-error approach. A second advantage, from the viewpoint of materials design, is that the effect of changing material properties (in particular the strength and toughness of both the matrix and/or the fibre-matrix interface) on the transitional ply thickness can be determined efficiently, simply by first calculating the resulting change in the R-curve. Similarly, the effect of operating at cryogenic temperatures can be efficiently assessed if the relevant material properties at those temperatures are known from direct measurements or can be reasonably estimated.

The presentation of this paper is organized as follows. The key features of the micromechanical model for a constrained layer are summarized in Section 2 using an explicit integration technique, as in our previous works [39, 40]. Representative results obtained by this approach are compared with the results reported previously in [8] that were obtained using an implicit algorithm, to demonstrate their equivalence, and to motivate the R-curve interpretation. The R-curve is then derived in Section 3, based on micromechanical modelling only within an embedded cell. In Section 4, this R-curve is employed in conjunction with finite element (FE) calculations of the energy release rate to predict the stability of through-thickness matrix cracking, according to the principle indicated in Fig. 1. Next, the dependence of the R-curve on matrix toughness and on fibre volume fraction is investigated, revealing a simple linear

relationship for the steady-state value. The effects of thermal residual stresses, which are ignored for simplicity in Sections 2-4, are investigated in Section 5. Finally, in Section 6, the R-curve approach is discussed relative to existing analytical models of ply cracking in laminates [27-36], highlighting the new insights provided by this approach.

2. Micromechanical modelling of through-thickness matrix cracking in a cross-ply laminate

An FE model of a cross-ply laminate is constructed that consists of three main parts, as shown in Fig. 2: (i) an inner layer incorporating a micromechanical model of one or more 90° plies; (ii) two adjacent constraining layers that are modelled as homogenized layers, and (iii) the interfaces between the inner layer and the outer constraining layers. The pertinent modelling assumptions are summarized in the sub-sections.

2.1 Micromechanical model of 90° inner layer

The formulation of the micromechanical model for the inner layer follows the approach developed originally by Melro et al. [15] for an unconstrained 90° layer (fibres are orthogonal to the main applied stress), i.e., a periodic representative volume element (RVE), and subsequently used by Arteiro et al. [8, 16] for cross-ply laminates. There are three constituents: fibres, matrix, and fibre-matrix interfaces; the relevant material properties are summarized below.

2.1.1 Carbon fibres

The fibres are assumed to have a circular cross-section, with a diameter of 5 μm, and to be linearly elastic and transversely isotropic relative to the fibre axis. The fibre volume fraction V_f is set at 0.6, which can be adjusted as discussed in Section 3.2. Within the 90° layer, the fibres are arranged in a random distribution that is representative of those observed in practice, following the approach in [15]; the importance of employing a random, rather than a regular (e.g., hexagonal) array for correct simulation of failure initiation, as well as strategies for generating representative random arrays, have been discussed by several authors [41-43]. The fibre axis is chosen to be the x-axis; the y-axis is in the direction of the in-plane loading along the 0° plies that is applied to cause through-thickness matrix cracking, and the z-axis is in the thickness direction, as indicated in Fig. 2(a). The relevant material properties are listed in Table 1, based on [8, 44, 45] which is representative of the IMS60 carbon fibres used in the experimental work [7].

2.1.2 Epoxy matrix

The matrix phase is assumed to be isotropic and to conform to the elasto-plastic with damage constitutive model recently formulated by Melro et al. [14, 15]. This model involves a linear elastic régime bounded by a pressure-dependent yield criterion, and subsequent parabolic hardening that correctly captures the detailed experimental measurements of Fielder et al. [46] for a representative epoxy under

126 various forms of loading. Damage in the epoxy matrix is modelled by a single damage variable that affects

127 only the Young's modulus once activated. Damage onset is defined by a damage activation function (Φ_m^d)

128 similar to the yield criterion, but with the tensile and compressive yield strengths replaced by ultimate

129 strengths. The Bazant-Oh [47] crack band model is employed to mitigate mesh-size dependency following

130 damage localization due to strain softening. The relevant material properties to implement this constitutive

131 model are listed in Table 2, which are considered here as standard values for typical Bisphenol-A type plain

132 epoxy resin as used in [7]. Further details of implementation are presented in the Supplementary Material

133 and in [8, 14].

134 *2.1.3 Fibre-matrix interfaces*

135   The fibre-matrix interface is characterized by the cohesive zone model (CZM) available in Abaqus

136 [48]. This involves a bilinear traction-displacement relation, with a high initial stiffness $K = 10^8 MPa/mm$

137 to enforce displacement continuity across the interface prior to damage. In the present work, damage onset

138 is governed by the maximum stress criterion [48]. Final failure is characterized by the Benzeggagh-Kenane

139 law [48] for mixed-mode failure. Values of the relevant properties are listed in Table 3.

140 **2.2 Homogenized outer constraining plies**

141   The outer layers in Fig. 2(a) are modelled as linear-elastic, orthotropic solids with the homogenized

142 properties represent 0° plies, to simulate the experimental set up of Saito et al. [7]. The relevant thermo-

143 mechanical properties are listed in Table 4, which are determined by FE homogenization of an RVE, as in

144 [49]. The interfaces between the inner and outer layers are modelled by CZM, using representative values

145 for interlaminar properties [8], which are listed in Table S1 in Supplementary Material.

146 **2.3 Model discretization, loading and boundary conditions**

147   The geometry shown in Fig. 2(a) is modelled using solid elements (C3D8R) [48] for matrix, fibres

148 and homogenized outer layers. The average element size within the inner layer is set to be 0.35 μm, to

149 generate a well-structured, high-quality mesh, as suggested in [17-20], based on a sensitivity analysis. The

150 fibre-matrix interface and the interface between inner and outer layers are modelled using cohesive

151 elements (COH3D8) [48] of zero thickness. The model length in the loading direction (*y*-axis) is 200 μm,

152 whereas the thickness in the fibre direction (*x*-axis) is approximately twice the average element size of the

153 inner layer, as in [8]. Periodic boundary conditions are applied in the *x* and *y* directions, using linear multi-

154 point constraints, to impose a homogenized strain, ε_{yy} that increases gradually to a final value of 2%.

155   As noted in Section 1, Abaqus/Explicit [48] is used in the present work, which allows a simpler

156 programming of the nonlinear constitutive model for the matrix phase as a user-defined subroutine

157   VUMAT. To assess the equivalence of the explicit approach with the implicit approach employed in [8], a

158   comparison is made for a thin-ply laminate with an inner layer of thickness $20 \ \mu m$ and outer layers of

159   thickness $75 \ \mu m$, employing the same material properties as [8] for model verification purposes. The results

160   are presented as Fig. S2 in the Supplementary Material, confirming the equivalence between the two

161   approaches.

162   *2.4 Simulation of through-thickness matrix cracking under increasing strain*

163   Figure 2(b) shows two representative images of the pattern of matrix cracking within an $30 \ \mu m$-

164   thick inner $90°$ layer, obtained in the present work. Microcracking is found to initiate at the fibre-matrix

165   interface (i.e. debonding), at a location where the inter-fibre spacing between two neighbouring fibres that

166   are aligned with the load axis (the *y*-axis) is relatively small, as indicated by a dashed box in Fig. 2(b). This

167   is in accord with the previous experimental and computational observations [7, 8, 50]. A through-thickness

168   matrix crack in micromechanical model is defined by the coalescence of at least two neighbouring

169   debondings, as defined in the experimental work [7]. The progression of through-thickness matrix cracking

170   is also similar to that previously reported in [7, 8], with a representative final pattern for an applied strain

171   of 2% being shown in Fig. 2(b). Figure 2(c) shows in more detail the evolution of the crack opening profile

172   for the through-thickness matrix crack indicated by the dashed box in Fig. 2(b). The localized crack opening

173   displacement (COD) is measured as the relative displacement between adjacent nodes after the occurrence

174   of microcracking, as in [8]. This progression of the crack opening profile under increasing applied strain

175   values is reported here for the first time.

176   The increasing values of COD for the near tip opening profiles appear to be indicative of an

177   increasing crack growth resistance with increasing crack length. An initial estimate of the crack growth

178   resistance G^R, based on the tip-to-tip crack length $2a$ of a through-thickness matrix crack and the maximum

179   COD for various levels of strain, as obtained from Fig. 2(c), is shown in Fig. 2(d), which clearly indicates

180   an increasing crack growth resistance. The details of the calculation are documented in the Supplementary

181   Material. This novel interpretation of the simulation results will be explored more quantitatively in the

182   present work by independently deriving the R-curve based on micromechanical modelling in Section 3.

183   **3. Crack growth resistance curve (R-curve) method**

184   *3.1 Micromechanical calculation of the R-curve*

185   Unlike the fracture toughness, which can be regarded as a material property under conditions of

186   small-scale yielding [37, 38], the R-curve is not strictly a material property: it depends on the configuration

187   (i.e., the specimen geometry, initial crack length, type of loading, etc. [51, 52]), although in practice this

188   dependence may be masked by the scatter in experimental measurements. This configuration dependence

189   is revealed, however, by analytical models where the material property characterizing failure is specified

190   in the form of a traction-separation law [53], and in experimental work involving large-scale bridging [51,

191   52]. Accordingly, it is important to generate an R-curve based on a configuration that is as close as possible

192   to the intended application of the R-curve for predictive purposes.

193   In the present context, an attractive option for generating the R-curve computationally is to use two

194   neighbouring fibres, such as those in the neighbourhood of the initiation site in Fig. 2(b), as load application

195   points, with equal and opposite point forces applied to those two fibres to initiate failure at the fibre-matrix

196   interface. It was found, however, that this approach resulted in inelastic deformation of the matrix around

197   those fibres that is not directly associated with the crack initiation and crack growth process, and the

198   contribution of this extraneous energy dissipation to the work of fracture could not readily be quantified.

199   These results are presented in the Supplementary Material.

200   Instead, the configuration shown in Fig. 3 was found to be more tractable for generating an

201   appropriate R-curve. In this figure, the entire model consists of 90° ply material only. However, for

202   computational efficiency, micromechanical modelling is limited to only a central region of the specimen,

203   while the remainder is modelled with homogenized (elastic) properties, as indicated in Fig. 3, in accordance

204   with the embedded cell approach [11]. The size of this embedded cell must be such as to fully capture all

205   inelastic deformation. This requirement must be verified at the end of a simulation. In the present work, the

206   height of the embedded cell in the y-direction (the direction of loading) was taken to be $h = 76\ \mu m$, which

207   was found to satisfy the above requirement, as will be seen below. The specimen length in the z-direction

208   (the direction of crack growth) was taken to be $w = 420\ \mu m$, which proved to be large enough for the R-

209   curve to reach a plateau value G_{ss}^{R} corresponding to steady-state crack growth. The same material properties

210   and element types as described in Section 2 were again employed. The displacement field is assumed to be

211   continuous across the interfaces between the embedded cell and the homogenized outer portions. The

212   average element size within the embedded cell is $0.35\ \mu m$ approximately, and the element size increases

213   gradually to $6.3\ \mu m$ in the homogenized portions. As in Section 2.3, the model thickness in the x-direction

214   (the fibre axis) is twice the average element size within the embedded cell, and periodic boundary conditions

215   are applied to the faces normal to the x-axis.

216   To avoid the difficulties noted above with point loading of fibres, the model shown in Fig. 3 includes

217   a pre-existing crack of length $a_0 = 4\ \mu m$, created by initially debonding the relevant nodes. This length is

218   chosen on the basis that it is equal to half of the shortest tip-to-tip crack length that can be reliably measured

219   experimentally or in simulations [7, 8], as indicated in Figs. 2(b,c), and for which the crack can reasonably

220 be approximated as a straight centre crack for the purposes of calculating the energy release rate, keeping

221 in mind that the initial crack at the fibre-matrix interface has a curvature dictated by the fibre diameter,

222 which is $5\ \mu m$ for the present simulations. To generate the R-curve, this pre-crack is opened by applying

223 specified displacements on the face $z = 0$: all nodes with $y > 0$ are given a specified vertical displacement

224 $u_y(y > 0, z = 0)$, whereas all nodes below the crack, with $y < 0$, are held fixed, i.e. $u_y(y < 0, z = 0) =$

225 0. The resulting nodal forces for $y > 0$ are summed to obtain the crack opening force P, whereas the crack

226 mouth opening displacement is given by $\Delta = u_y(y > 0, z = 0) - u_y(y < 0, z = 0)$.

227 A representative load-displacement $(P - \Delta)$ curve obtained in this manner is shown in Fig. 4(a).

228 This curve includes some periodical unloadings that are intended to check that the unloading response is

229 linearly elastic, with the unloading curves returning to the origin, as required to ensure the validity of the

230 LEFM formula [54] for calculating the crack growth resistance, viz., $G^R = \frac{1}{2}bP^2\partial C/\partial a$, where b denotes the

231 specimen thickness (in the x-direction in the present case) and $C = P/\Delta$ the compliance. To obtain the crack

232 length a, the crack tip is identified by searching for the element furthest away from the face $z = 0$ at which

233 the damage variable has reached the value 1, corresponding to complete failure; the crack length is then

234 taken as the distance from the crack tip to the face $z = 0$.

235 Because of the random distribution of fibres built into the model, slightly different results are

236 obtained from different simulation runs. Figure 4(b) shows the combined results obtained from five

237 different simulations, involving five different realizations of random fibre distributions, but all for the same

238 volume fraction. The scatter in these results is attributable to the randomness of the fibre distributions, all

239 other properties being deterministic. For predictive purposes, the raw results from the simulations are fitted

240 with a rational polynomial of second order, to obtain the continuous curve shown in Fig. 4(b) for $G^R(a)$.

241 With the present approach, this curve necessarily starts from the assumed initial crack length $a_0 = 4\ \mu m$.

242 However, the smallest ply thickness that can currently be achieved with tow-spreading technology is around

243 $15\ \mu m$ [21, 22], so that this assumed initial crack length is not unduly restrictive in practice.

244 Figure 4(c) illustrates the progression of deformation and crack growth under increasing load. It can

245 be seen that the crack path often follows the fibre-matrix interface, and proceeds discontinuously, with

246 heavily deformed but unbroken matrix ligaments bridging the crack behind the crack tip. These

247 observations from the present micromechanical modelling are in accord with previous experimental and

248 computational results [7-20, 50]. Thus, the crack path is not straight at the microscopic level. Figure 4(d)

249 shows representative maps of the damage activation variable (Φ_m^d) for two crack lengths. It can be seen

250 that the damage zone is fully contained within the embedded cell, even for the longer crack length of $80\ \mu m$,

corresponding to steady-state crack growth, indicating that the selected size for the embedded cell is sufficient to correctly capture the R-curve.

3.2 Effect of matrix toughness and fibre volume fraction on crack growth resistance

The influence of various material properties on through-thickness matrix cracking can now be investigated by first determining their influence on the R-curve. To illustrate the procedure, consider first the influence of the matrix fracture toughness G_c, all other material properties and modelling assumptions being kept the same. Figure 5(a) shows the R-curves obtained for $G_c = 80,160,240 \, J/m^2$, as well as the previous curve in Fig. 4(b) for $G_c = 120 \, J/m^2$ which serves as the baseline. It can be seen that the steady-state value G_{ss}^R, and the extent of crack growth required to reach the steady state, both increase with increasing G_c. Recalling that crack growth involves debonding at the fibre-matrix interface, with the crack being bridged by matrix ligaments behind the crack tip, it appears reasonable to expect that the steady-state value G_{ss}^R can be estimated from a simple rule-of-mixtures (RoM) formula involving both the interfacial toughness (G_{Ic}^{int}) and the matrix toughness, as follows

$$G_{ss}^R = V_f G_{Ic}^{int} + \left(1 - V_f\right)G_c. \tag{1}$$

Figure 5(b) shows that this simple formula indeed provides a good estimate for G_{ss}^R, at least within the investigated range for G_c. This in turn suggests a useful approach for estimating G_{ss}^R in situations where measured values of G_c may not be available but can be reasonably estimated.

Next, Fig. 5(c) shows the R-curves for fibre volume fractions $V_f = 0.45$ and 0.55 in addition to the baseline value 0.6 employed previously in Fig. 4(b), and retaining the same values for all other parameters. It can be seen that the initial slope of the R-curve ($\partial G^R/\partial a$) and the final steady-state value G_{ss}^R increase with decreasing V_f. Figure 5(d) shows that the simple formula in Eq. (1) again provides a reasonable estimate for G_{ss}^R, at least for the range of V_f investigated here that is representative of the values encountered in practice. The increase in G_{ss}^R is consistent with an increased dissipation due to wider bridging ligaments as V_f decreases (the fibre diameter remaining fixed).

4. Stability of through-thickness matrix cracking

Having obtained the R-curve for the crack growth resistance $G^R(a)$ as in Fig. 4(b), the next requirement is to determine the energy release rate $G(a)$ as a function of the half-crack length a for the configuration shown in Fig. 6(a).

4.1 Energy release rate

To determine $G(a)$ the inner layer is modelled as a homogeneous layer, with the same lamina properties as listed in Table 4 for the outer plies, but with the fibre orientation now parallel to the x-axis, instead of the y-axis. The deformation in Fig. 6(a) is assumed to be plane strain ($\varepsilon_{xx} = 0$). The energy release rate can then be expressed as follows [29, 55]

$$G(a) = \Lambda \sigma_{yy}^2 \pi a f\left(\frac{a}{t_1}, \frac{t_2}{t_1}, \frac{E_T}{E_L}, \dots\right) \tag{2}$$

where $\Lambda = \left(\frac{1}{E_T} - \frac{v_L}{E_L}\right)$, $\sigma_{yy} = \varepsilon_{yy}/\Lambda$, which denotes the stress within the inner layer in an uncracked laminate, under an applied strain ε_{yy}. In this expression, the function f can be regarded as a nondimensional correction factor that depends on several configurational parameters and material properties. In the limit of very small cracks, the influence of the outer ply thickness and stiffness becomes negligible, i.e., $f(a/t_1 \ll 1) = 1$, and $G(a)$ reduces to $G(a) = \Lambda \sigma_{yy}^2 \pi a$, as which is appropriate for a centre crack of length $2a$ in a transversely isotropic material under plane strain. Values of $G(a)$ can be readily determined computationally, e.g. by the virtual crack closure technique (VCCT) available in Abaqus [48]. The results for the dependence of $G(a)$ on crack size are shown in Fig. 6(b), using the following dimensionless form:

$$g\left(\frac{a}{t_1}\right) = \frac{G(a)}{\Lambda \sigma_{yy}^2 \pi t_1} = \frac{a}{t_1} f\left(\frac{a}{t_1}, \frac{t_2}{t_1}, \frac{E_T}{E_L}, \dots\right) \tag{3}$$

These results were obtained for a fixed value of the constraining layer thickness $t_2 = 480 \ \mu m$, as in the experimental work [7]. It can be seen that $g(a/t_1)$ is only weakly dependent on the modulus ratio E_T/E_L in the range $0.02-0.1$; it was also found to be insensitive to the value of the inner-layer thickness $2t_1$ in the range $40 - 160 \ \mu m$, and insensitive to the Poisson ratios within the range encountered in practice for CFRP. Furthermore, the present results for orthotropic layers are very close to the results for isotropic inner and outer layers, with Young's moduli equal to E_T and E_L respectively [29, 55]. The important feature in Fig. 6(b) is that $g(a/t_1)$ decreases when the crack size exceeds 70% of the inner layer thickness, which indicates the constraining action of the stiff outer layers, as noted in previous work [29]. For the subsequent analysis, the numerical results for $g(a/t_1)$, for $E_T/E_L = 0.05$, were fitted to a fourth-order polynomial in a/t_1. More information is given in the Supplementary Material.

4.2 Predicting the progression of through-thickness matrix cracking

The progression of through-thickness matrix cracking can now be predicted by the procedure indicated in Fig. 1, which is illustrated in more detail in Fig. 6(c). Crack growth is stable if the gradient of the crack-growth curve is less than the gradient of the crack growth resistance curve, i.e., $\frac{\partial G}{\partial a} < \frac{\partial G^R}{\partial a}$, where

308   G, G^R, a denote respectively the crack-growth energy release rate, crack-growth resistance, and crack length

309   (or half-crack length for centre cracks). Unstable crack growth occurs when the gradient of the crack-

310   growth curve exceeds the gradient of the crack growth resistance curve, i.e., $\frac{\partial G}{\partial a} > \frac{\partial G^R}{\partial a}$.

311   Consider first the case where the inner layer thickness is $40 \ \mu m$, corresponding to a single ply in

312   the experimental set up, i.e. $n = 1$ for the $[0_m, 90_{n/2}]_s$ laminates investigated by Saito et al. [7]. The curves

313   of $G(a)$ for that inner-layer thickness $2t_1$ are shown in red in Fig. 6(c), for various values of ε_{yy}. It can be

314   seen that the crack growth criterion $G = G^R$ is first satisfied when $\varepsilon_{yy} = 0.7\%$, and the half-crack length

315    $a_0 = 4 \ \mu m$. This initial value of crack length a_0 corresponds to the shortest crack length, corresponding

316   one fibre-matrix disbond, for which the R-curve is available, as discussed above in Section 3. It is clear

317   from Fig. 6(c) that for this initial crack length, $\partial G/\partial a < \partial G^R/\partial a$, thus crack growth is predicted to be

318   stable [37, 38]. Next, as the applied strain increases to $\varepsilon_{yy} = 1\%$, the crack grows to a length of $a = 7 \mu m$

319   and $\partial G/\partial a < \partial G^R/\partial a$, i.e., crack growth is still predicted to be stable. Proceeding in this manner, one can

320   construct a continuous curve of crack length versus applied strain, which is shown as the solid red curve in

321   Fig. 7(a). The crack length is normalized by the layer thickness to facilitate comparison with the

322   experimental results in [7] which are shown as data points in Fig. 7. It can be seen that the R-curve method

323   correctly captures the average behaviour observed experimentally, and correlates well with the results

324   obtained in the present work by the micromechanical simulation described in Section 2, which are shown

325   by the dashed curve in Fig. 7. Stable crack growth is always predicted until full through-thickness

326   penetration at $\varepsilon_{yy} = 1.7\%$.

327   Consider next an inner layer thickness $2t_1 = 160 \ \mu m$, corresponding to $n = 4$ for the experimental

328   laminate [7]. It can be seen from Fig. 6(c) that the crack growth criterion is again satisfied at $\varepsilon_{yy} = 0.7\%$

329   for $a_0 = 4 \ \mu m$, and growth is predicted to be initially stable as $\partial G/\partial a < \partial G^R/\partial a$. However, when the

330   applied strain has increased to $\varepsilon_{yy} = 1\%$, and the half-crack length has reached $a = 11 \ \mu m$, further crack

331   growth is predicted to be unstable, because now $\partial G/\partial a > \partial G^R/\partial a$. The full predicted response is shown

332   by the solid blue curve in Fig. 7(b), which can again be seen to correctly capture the behaviour recorded

333   experimentally, as well as the results obtained by the micromechanical simulations described in Section 2.

334   Finally, for the intermediate layer thickness investigated experimentally, $2t_1 = 80 \ \mu m, n = 2$, the

335   predicted behaviour is slightly more complicated. Crack growth is again predicted to initiate at $\varepsilon_{yy} = 0.7\%$

336   for $a_0 = 4 \ \mu m$, and to be initially stable because $\partial G/\partial a < \partial G^R/\partial a$, as can be seen from the green curves

337   in Fig. 6(c). Next, when the applied strain has increased to $\varepsilon_{yy} = 1\%$, and the crack length has reached

338    $a = 11\ \mu m$, subsequent growth is predicted to be unstable, because $\partial G/\partial a > \partial G^R/\partial a$. But now this

339   inequality only applies for a limited extent of crack growth: as the crack grows, the value of G eventually

340   decreases and intersects the G^R curve for $a = 32\ \mu m$ ($a/t_1 = 0.8$), and $\partial G/\partial a < \partial G^R/\partial a$ at that point,

341   which indicates crack arrest. Further crack growth beyond that point requires an increasing applied strain.

342   This subsequent growth is predicted to be stable, because $\partial G/\partial a < 0$ beyond $a/t_1 \approx 0.7$, whereas

343    $\partial G^R/\partial a \geq 0$, so that the stability criterion $\partial G/\partial a < \partial G^R/\partial a$ is always satisfied until full through-

344   thickness penetration at $\varepsilon_{yy} = 1.4\%$. This predicted response is shown by the continuous green curve in

345   Fig. 7(b), and it can be seen to be in reasonable agreement with the experimental observations in [7], as

346   well as the results of micromechanical simulations of the present work.

5. Through-thickness matrix cracking at cryogenic temperature

348   Thermal residual stresses arise at two length scales in fibre-composite laminates [4, 56]: intra-ply

349   residual stresses arise between the fibres and matrix within a ply, due to their different coefficients of

350   thermal expansion (CTE); inter-ply residual stresses arise between plies of differing orientations within a

351   laminate, due to the variation in the homogenized CTE with orientation. The inter-ply residual stresses are

352   uniformly distributed across the ply thickness, and can be calculated by using conventional lamination

353   theory [57] or FE, whereas the intra-ply residual stresses require micromechanical modelling. To account

354   for the effects of thermal residual stresses on the R-curve approach for predicting through-thickness crack

355   growth, two distinct calculations are required: first, the change in the R-curve must be determined, based

356   on micromechanical modelling, and secondly, the change in the energy release rate as a function of applied

357   strain ε_{app} must be evaluated, by first calculating the inter-ply residual stress or strain ε_{th}, based on

358   lamination theory. Furthermore, the change in material properties with decreasing temperature must also

359   be taken into account, most notably the change in matrix fracture toughness. These steps are addressed in

360   turn in the following sub-sections.

5.1 Effect of intra-ply residual stresses on the crack growth resistance curve

362   The implementation of the FE model described in Section 3.1 is modified by including a preliminary

363   step, henceforth referred to as Step 1, to simulate a temperature change ΔT prior to applying an external

364   load in Step 2, while retaining all other model specifications and material properties as previously described

365   in Section 3. For illustrative purposes, ΔT is chosen here to be -278K, corresponding to the temperature

366   drop from room temperature (RT) to liquid hydrogen temperature (LH$_2$). At the completion of Step 1, the

367   resulting residual stress field is similar to that reported in several previous micromechanical simulations of

368   unconstrained unidirectional plies [10, 41]. Consequently, this residual stress field will not be documented

369   in detail here, except to note (i) the stress everywhere remains below the damage-inducing levels, both in

370   the matrix and at the fibre-matrix interface, for the current choice of ΔT and material parameters; and (ii)

371   the interfacial normal stress is predominantly compressive (see Fig. S8 of the Supplementary Material),

372   suggesting an increased resistance to crack growth due to delayed fibre-matrix debonding.

373   The residual stress field from Step 1 is retained as an initial stress field for Step 2 of determining

374   the R-curve. For that purpose, an initial edge crack of length $a_0 = 4\ \mu m$ is again introduced and opened as

375   previously described in Section 3.1 and Fig 3. The results are shown in Fig. 8(a), for the same four values

376   of matrix toughness G_c that were previously used to generate the results in Fig. 5(a). The solid curves in

377   Fig. 8(a) again represent a rational polynomial fit to the data obtained from five separate simulations, for

378   each value of G_c. The R-curves previously derived without considering the thermal residual stresses are

379   shown as dashed curves for comparison purposes. It can be seen that the residual stresses indeed lead to an

380   increased crack growth resistance. Furthermore, the steady-state resistance G_{ss}^R again increases linearly with

381   increasing G_c, and there is an increasing difference with the previously calculated values of G_{ss}^R with

382   increasing G_c, as shown in Fig. 8(b), which is not captured by the RoM in Eq. (1), but Eq. (1) nevertheless

383   continues to provide a useful estimate for practical purposes.

384   *5.2 Effect of inter-ply residual stresses on the energy release rate*

385   Turning next to the calculation of the energy release rate for the configuration shown in Fig. 6(a), it

386   is noted that Eq. (2) is still applicable provided that σ_{yy} is taken as the sum of the thermal residual stress

387   and the applied stress, or equivalently, that ε_{yy} is interpreted as the total strain ε_{yy}^{total} on the 90° layer,

388   consisting of an residual strain at the ply level ε_{yy}^{th}, plus an applied strain ε_{yy}^{app} at LH$_2$:

389      $$\varepsilon_{yy}^{total} = \varepsilon_{yy}^{th} + \varepsilon_{yy}^{app}. \tag{4}$$

390   The calculation for ε_{yy}^{th} is documented in the Supplementary Material.

391   *5.3 Predicting through-thickness crack growth at cryogenic temperature*

392   Having determined the effects of thermal residual stresses on both the R-curve and the energy

393   release rate, we can now predict the progression of through-thickness matrix cracking as in Section 4. The

394   predicted responses are shown as the solid curves in Figs. 9(a-c), for the three 90° layer thicknesses and

395   four values of G_c previously considered in Section 4. These predictions are compared with the results

396   obtained by modifying the micromechanical model in Section 2 to include a preliminary step (Step 1)

397   corresponding to a temperature change $\Delta T = -278K$, prior to applying an external load. These simulation

398   results here serve the role of experimental results, in the absence of direct experimental observations at

399   LH$_2$, and they are shown as the dashed lines in Figs. 9(a-c), but for only two values of matrix toughness

400     $G_c = 120$ and $240\,J/m^2$ due to the laborious computational effort. It can be seen that the predicted crack

401   growth based on the R-curve approach is again in good agreement with the more laboriously obtained

402   micromechanical simulations.

403   In Figs. 9(a-c), the dotted vertical lines indicate the thermal strain ε_{yy}^{th} on $90°$ layer at the completion

404   of Step 1. Thus, the predicted behaviour as a function of applied strain can be visualized by focussing on

405   the results to the right of these dotted lines. In particular, it is of interest to note the value of applied strain

406   that is required to achieve full-thickness cracking, which is re-plotted in Fig. 9(d). For a given value of G_c,

407   crack growth becomes progressively more unstable as the ply thickness increases, thereby resulting in full-

408   thickness cracking at a lower applied strain; on the other hand, for a given ply thickness, growth becomes

409   more stable as G_c increases, so that a higher applied strain is required for full-thickness cracking. These

410   results provide a basis for quantifying the potential benefits of the nano-toughening techniques, as

411   developed in [58, 59], in conjunction with tow-spreading technology for facilitating the design and

412   optimization of the composite vessels for storing cryogenic fuels.

5.4 Effect of changing matrix toughness with decreasing temperature

414   Variations in matrix and interface strength and toughness are generally very laborious to

415   characterize experimentally [58, 59], on the one hand, but are expected to have a significant influence on

416   the failure behaviour, on the other. To illustrate how the present work provides an efficient approach for

417   estimating matrix-cracking behaviour at cryogenic temperatures, consider the case where the matrix

418   toughness decreases from a RT value $G_c = 120\,J/m^2$, to an assumed lower value $G_c = 60\,J/m^2$ at LH2 as

419   measured in [58] at cryogenic temperature and as indicated by the arrow in Fig 8(b) (all other material

420   properties being assumed to retain their RT values, for simplicity). Figures 10(a-c) shows the predicted

421   behaviour for through-thickness matrix cracking, based on (i) the RT value of G_c, and ignoring thermal

422   residual stresses for which the total strain is simply the applied strain $\varepsilon_{yy}^{total} = \varepsilon_{yy}^{app}$, and (ii) the LH2 value

423   of G_c, and accounting for thermal residual stresses for which the total strain is the sum of thermal residual

424   strain and applied strain as defined by Eq. (3). It is shown that the ply thickness for which through-thickness

425   matrix cracking transitions from stable to unstable growth is smaller for case (ii) relative to case (i), due to

426   the lower G_c at LH2; on the other hand, the applied strain for causing full-thickness cracking is significantly

427   lower for case (ii) relative to case (i) (see Fig. 10(d)), due to the high inter-ply residual strain at LH2. This

428   is clearly an important observation from the viewpoint of exploiting the potential benefits of toughened thin

429   plies for cryogenic applications.

6. Discussion

6.1 Contribution to computational efficiency for micromechanical simulations

Micromechanical modelling is becoming an essential tool to characterize the deformation and failure mechanisms within a ply, providing insights and inputs for the next levels (mesoscale and macroscale) in a structured multiscale modelling framework leading to a virtual testing pyramid for fibre-composite structures [18]. The recent micromechanical model of Arteiro et al. [8] correctly captures the experimentally observed transition from unstable to stable through-thickness crack growth in the 90° ply of a cross-ply laminate [7]. However, the specification of material properties in [8] requires no fewer than 35 parameters, as well as two stress-strain curves characterizing the plastic deformation and ultimate strength of the bulk epoxy, as derived from the experimental measurements [46] for tension and compression. The predicted response depends to some extent on each of these input parameters, but a detailed parametric analysis is clearly prohibitive. Even a more restricted study of the dependence on matrix and interfacial strength and toughness would be daunting, particularly if one were to also include an integrated modelling of the curing response for more accurate calculation of thermal residual stresses, as recently proposed in [20]. From this perspective, the present work contains two important contributions: first, a new approach has been proposed that can significantly reduce the computational burden, especially for a systematic parametric analysis; secondly, the simulations reported in [8, 16] have been extended to include the effects of residual stresses.

The benefit of the R-curve approach in reducing the computational burden has already been noted in Sections 4,5: once the R-curve has been generated the progression of through-thickness cracking can be readily predicted for any ply thickness, instead of requiring separate simulations for each ply thickness of interest. Furthermore, to determine the influence of various material parameters on the ply failure response, it is sufficient to determine their influence on the R-curve, which again reduces the required number of separate micromechanical simulations.

6.2 Comparison with theoretical models of ply cracking

Figure 11 shows the ply-thickness dependence of the failure strain for full through-thickness cracking, as derived from the present micromechanical modelling and experimental observations [7], as well as the ply cracking strain predicted by current theoretical models [27-36]. It is important to understand the scope as well as the limitations of both sets of predictions. Currently available theoretical models for ply cracking are based on (i) fracture mechanics [27-29], or (ii) finite fracture mechanics [31]. In the latter approach, there is no attempt to track the progression of cracking either through the thickness, or across the width, of a ply. Instead, a failure criterion is formulated by equating the change in configurational energy

15

(i.e. the sum of the stored elastic energy and the potential energy of the loading mechanism) due to a ply crack (spanning the full thickness and width of the ply) to the work of fracture for that area of crack. This is the approach originally adopted by Bailey et al. [1-3], and subsequently refined by several others on the basis of more refined stress analyses for evaluating the energy change, notably based on variational principles [31-35]. Regardless of the level of sophistication of the stress analysis, a finite fracture mechanics approach will necessarily predict a ply cracking strain that decreases as $1/\sqrt{2t_1}$ with increasing ply thickness $2t_1$, as shown by the dashed green curve in Fig. 11, and thus cannot account for the transition to the thick-ply régime, a limitation that was recognised in [2, 3].

Dvorak and Laws [29] have formulated a fracture mechanics approach that can account for the thin-to-thick-ply transition, as shown by the dashed red lines in Fig. 11, albeit based on postulating the existence of an effective initial crack whose precise shape and size are not known *a priori*, and employing simplified two-dimensional (2D) analyses that envisage the failure critical event as being either (i) crack growth across the ply thickness, for thick plies, or (ii) crack growth in a tunnelling mode (i.e. across the width of the laminate, for a crack spanning the full thickness of the transverse ply) for thin plies. In both cases, the relevant critical value of the energy release rate G_{mc} is assumed to be a constant, albeit having a different value for through-thickness cracking relative to crack growth across the laminate width (tunnelling mode). This approach necessarily predicts that through-thickness cracking is always unstable once it initiates (unless the pre-existing initial crack is assumed to span more than 70% of the ply thickness, cf. Fig. 6), and thus is unable to account for the experimental and computational observations of slow, stable growth in [7, 8]. Furthermore, G_{mc} has the status of an empirical constant that is determined by curve fitting the experimentally measured data for failure strain versus ply thickness. Although this empirical value of G_{mc} will necessarily depend on the fracture toughness for the bulk matrix, there is no explicit relation between the two, and hence no simple way of predicting the beneficial effects of matrix toughening, for example. The dashed curves in Fig. 11 are based on assuming $G_{mc} = 220 \, J/m^2$ as originally used in [29, 34]. It should be noted that the energy change driving the tunnelling mode is essentially the same as that considered in the finite fracture mechanics approach; the difference between the dashed curves in Fig. 11 can be attributed to differences in the stress analyses for calculating this energy change.

By contrast to the models in [27-30], the micromechanical simulations do not assume a pre-existing crack. Instead, cracking is shown to initiate by fibre-matrix debonding, as shown earlier in Fig. 2(b). This pattern of initiation and subsequent growth correlates closely with experimental observations [7, 28], whereas experimental evidence of pre-existing cracks, as required by the fracture mechanics models [27-29], has never been reported. Another difference with the present work is that the models in [27-29, 31-35]

16

have always assumed a single value for the fracture toughness, rather than a rising R-curve, as derived here in Section 3. This R-curve behaviour has been shown to account for the transition to slow, stable through-thickness crack growth with decreasing ply thickness. The predicted strain for full through-thickness cracking based on the present R-curve approach is displayed as the solid curve in Fig. 11, showing good agreement with experimental observations [7] and micromechanical simulation results. A limitation of the present micromechanical model, however, is that it can only characterize through-thickness cracking, and therefore it cannot predict the ply-cracking strain if the failure critical event is crack growth across the laminate width (tunnelling mode). However, these predictions for through-thickness cracking are most valuable for laminate design, particularly in the context of ensuring antileakage properties. Future work is required to clarify the relation between the resistance to through-thickness cracking and the so-called matrix cracking toughness that characterizes the tunnelling mode of ply cracking. The steady-state crack resistance for through-thickness cracking, G_{ss}^R, has been shown in the present work to be well approximated by a RoM formula, Eq. (1), and it is therefore necessarily less than the epoxy matrix toughness, G_c, whereas the matrix-cracking toughness G_{mc}, which determined empirically as discussed above, is generally much larger than G_c; for example, the dashed curves in Fig. 11 employed a value of G_{mc} that is approximately twice the fracture energy for a typical epoxy matrix. The reason for this relatively large value of the matrix-cracking toughness is not entirely clear; it may be due to fibre-bridging, which cannot be capture with the present micromechanical model.

7. Conclusions

A new concept has been proposed and demonstrated to account for the experimental observations of slow, stable cracking across the thickness of the 90° ply in a cross-ply laminate, when the ply thickness is reduced to 40 µm. The proposed explanation is that through-thickness cracking proceeds under an increasing crack growth resistance characterized by an R-curve, after initiating in a natural manner at the fibre-matrix interface. This explanation has been substantiated by employing a high-fidelity micromechanical model to generate the R-curve for crack growth in an unconstrained 90° ply. The R-curve is then employed to predict the progression and stability of through-thickness cracking based on principles of fracture mechanics. The predicted crack growth correctly captures both the experimental observations and the simulation results, showing a transition from stable growth to unstable growth with increasing 90°-layer thickness.

One major benefit of the R-curve approach is that only one micromechanical simulation is required for generating the R-curve, which can then be employed to predict the progression of crack growth for inner layers of any thickness, instead of requiring a separate simulation for each layer thickness of interest. This

considerably reduces the computational burden for micromechanical simulations, which is particularly valuable for conducting detailed parametric studies to examine the dependence of ply cracking on various material properties. As an illustrative example, the dependence on matrix toughness has been investigated. The results show that the steady-state value of crack growth resistance appears to increase linearly with increasing matrix toughness, and this linear increase is closely approximated by a simple rule-of-mixtures formula that also involves the interfacial toughness and fibre volume fraction.

This first demonstration of the R-curve approach can be extended to account for the effects of residual stresses, which arise at two distinct length scales. The intra-ply residual stresses must be evaluated using micromechanical modelling, and they only affect the R-curve, whereas the inter-ply residual stresses must be evaluated from ply-level (mesoscale) modelling, and they only affect the energy release rate for through-thickness cracking. It has been shown that the steady-state crack growth resistance again follows a linear increase with increasing matrix toughness. The existence and identification of such simple relationships can further reduce the computational burden for systematic parametric studies and sensitivity analyses based on micromechanical simulations. The new insights provided by these simulations relative to currently available theoretical models for ply cracking have been discussed.

Declaration of competing interest

The authors declare that they have no known competing financial interests or personal relationships that could have appeared to influence the work reported in this paper.

Acknowledgements

References

[1] K. Garrett, J. Bailey, Multiple transverse fracture in 90 cross-ply laminates of a glass fibre-reinforced polyester, J. Mater. Sci. 12(1) (1977) 157-168.
[2] A. Parvizi, K. Garrett, J. Bailey, Constrained cracking in glass fibre-reinforced epoxy cross-ply laminates, J. Mater. Sci. 13(1) (1978) 195-201.
[3] J. Bailey, P. Curtis, A. Parvizi, On the transverse cracking and longitudinal splitting behaviour of glass and carbon fibre reinforced epoxy cross ply laminates and the effect of Poisson and thermally generated strain, Proc. R. Soc. Lond. A 366(1727) (1979) 599-623.
[4] S.L. Ogin, P. Brondsted, J. Zangenberg, Composite materials: constituents, architecture and generic damage, in: R. Talreja, J. Varna (Eds.), Modeling Damage, Fatigue and Failure of Composite Materials, Elsevier 2016, pp. 3-23.
[5] V. Singh, Evolution of multiple matrix cracking, in: R. Talreja, J. Varna (Eds.), Modeling Damage, Fatigue and Failure of Composite Materials, Elsevier 2016, pp. 143-171.
[6] D.L. Flaggs, M.H. Kural, Experimental determination of the in situ transverse lamina strength in graphite/epoxy laminates, J. Compos. Mater. 16(2) (1982) 103-116.
[7] H. Saito, H. Takeuchi, I. Kimpara, Experimental evaluation of the damage growth restraining in 90° layer of thin-ply CFRP cross-ply laminates, Adv. Compos. Mater. 21(1) (2012) 57-66.
[8] A. Arteiro, G. Catalanotti, A.R. Melro, P. Linde, P.P. Camanho, Micro-mechanical analysis of the in situ effect in polymer composite laminates, Compos. Struct. 116 (2014) 827-840.
[9] E. Totry, C. González, J. Llorca, Prediction of the failure locus of C/PEEK composites under transverse compression and longitudinal shear through computational micromechanics, Compos. Sci. Technol. 68(15-16) (2008) 3128-3136.
[10] T.J. Vaughan, C.T. McCarthy, Micromechanical modelling of the transverse damage behaviour in fibre reinforced composites, Compos. Sci. Technol. 71(3) (2011) 388-396.
[11] L.P. Canal, C. González, J. Segurado, J. Llorca, Intraply fracture of fiber-reinforced composites: Microscopic mechanisms and modeling, Compos. Sci. Technol. 72(11) (2012) 1223-1232.

[12] H. Saito, H. Takeuchi, I. Kimpara, A study of crack suppression mechanism of thin-ply carbon-fiber-reinforced polymer laminate with mesoscopic numerical simulation, J. Compos. Mater. 48(17) (2014) 2085-2096.

[13] M. Herráez, D. Mora, F. Naya, C.S. Lopes, C. González, J. Llorca, Transverse cracking of cross-ply laminates: A computational micromechanics perspective, Compos. Sci. Technol. 110 (2015) 196-204.

[14] A.R. Melro, P.P. Camanho, F.M. Andrade Pires, S.T. Pinho, Micromechanical analysis of polymer composites reinforced by unidirectional fibres: Part I – Constitutive modelling, Int. J. Solids Struct. 50(11-12) (2013) 1897-1905.

[15] A.R. Melro, P.P. Camanho, F.M. Andrade Pires, S.T. Pinho, Micromechanical analysis of polymer composites reinforced by unidirectional fibres: Part II – Micromechanical analyses, Int. J. Solids Struct. 50(11-12) (2013) 1906-1915.

[16] A. Arteiro, G. Catalanotti, A.R. Melro, P. Linde, P.P. Camanho, Micro-mechanical analysis of the effect of ply thickness on the transverse compressive strength of polymer composites, Compos. - A: Appl. Sci. Manuf. 79 (2015) 127-137.

[17] Q. Sun, Z. Meng, G. Zhou, S.-P. Lin, H. Kang, S. Keten, H. Guo, X. Su, Multi-scale computational analysis of unidirectional carbon fiber reinforced polymer composites under various loading conditions, Compos. Struct. 196 (2018) 30-43.

[18] A. Arteiro, G. Catalanotti, J. Reinoso, P. Linde, P.P. Camanho, Simulation of the mechanical response of thin-ply composites: from computational micro-mechanics to structural analysis, Arch. Comput. Methods Eng. 26(5) (2018) 1445-1487.

[19] Q. Sun, G. Zhou, Z. Meng, M. Jain, X. Su, An Integrated computational materials engineering framework to analyze the failure behaviors of carbon fiber reinforced polymer composites for lightweight vehicle applications, Compos. Sci. Technol. 202 (2021).

[20] X. Hui, Y. Xu, W. Zhang, An integrated modeling of the curing process and transverse tensile damage of unidirectional CFRP composites, Compos. Struct. 263 (2021).

[21] R. Amacher, J. Cugnoni, J. Botsis, L. Sorensen, W. Smith, C. Dransfeld, Thin ply composites: Experimental characterization and modeling of size-effects, Compos. Sci. Technol. 101 (2014) 121-132.

[22] J. Galos, Thin-ply composite laminates: a review, Compos. Struct. 236 (2020).

[23] S. Sihn, R. Kim, K. Kawabe, S. Tsai, Experimental studies of thin-ply laminated composites, Compos. Sci. Technol. 67(6) (2007) 996-1008.

[24] N. Liu, B. Ma, F. Liu, W. Huang, B. Xu, L. Qu, Y. Yang, Progress in research on composite cryogenic propellant tank for large aerospace vehicles, Compos. - A: Appl. Sci. Manuf. 143 (2021).

[25] J. Hohe, A. Neubrand, S. Fliegener, C. Beckmann, M. Schober, K.-P. Weiss, S. Appel, Performance of fiber reinforced materials under cryogenic conditions—A review, Compos. - A: Appl. Sci. Manuf. 141 (2021).

[26] J. Hohe, M. Schober, S. Fliegener, K.-P. Weiss, S. Appel, Effect of cryogenic environments on failure of carbon fiber reinforced composites, Compos. Sci. Technol. 212 (2021).

[27] F. Crossman, A. Wang, The dependence of transverse cracking and delamination on ply thickness in graphite/epoxy laminates, Damage in composite materials: basic mechanisms, accumulation, tolerance, and characterization, ASTM International1982.

[28] A. Wang, Fracture mechanics of sublaminate cracks in composite laminates, J. Compos. Technol. Res. 6(2) (1984).

[29] G.J. Dvorak, N. Laws, Analysis of progressive matrix cracking in composite laminates II. First ply failure, J. Compos. Mater. 21(4) (1987) 309-329.

[30] S. Ho, Z. Suo, Tunneling cracks in constrained layers, J. Appl. Mech. 60(4) (1993) 5.

[31] Z. Hashin, Finite thermoelastic fracture criterion with application to laminate cracking analysis, J. Mech. Phys. Solids. 44(7) (1996) 1129-1145.

[32] Z. Hashin, Analysis of cracked laminates: a variational approach, Mech. Mater. 4(2) (1985) 121-136.

[33] J.A. Nairn, S. Hu, J.S. Bark, A critical evaluation of theories for predicting microcracking in composite laminates, J. Mater. Sci. 28(18) (1993) 5099-5111.

[34] J.A. Nairn, Matrix microcracking in composites, in: R. Talreja, J.-A. M˚anson (Eds.), Polymer Matrix Composites, Elsevier Science2000, pp. 403-432.

[35] M. Hajikazemi, L.N. McCartney, W. Van Paepegem, M.H. Sadr, Theory of variational stress transfer in general symmetric composite laminates containing non-uniformly spaced ply cracks, Compos. - A: Appl. Sci. Manuf. 107 (2018) 374-386.

[36] J.-M. Berthelot, Transverse cracking and delamination in cross-ply glass-fiber and carbon-fiber reinforced plastic laminates: Static and fatigue loading, Appl. Mech. Rev. 56(1) (2003) 111-147.

[37] D. Broek, Elementary engineering fracture mechanics, Springer Science & Business Media1982.

[38] T.L. Anderson, Fracture mechanics: fundamentals and applications, CRC press2017.

[39] C.H. Wang, A.J. Gunnion, A.C. Orifici, A. Rider, Residual strength of composite laminates containing scarfed and straight-sided holes, Compos. - A: Appl. Sci. Manuf. 42(12) (2011) 1951-1961.

[40] J. Ahamed, M. Joosten, P. Callus, S. John, C.H. Wang, Ply-interleaving technique for joining hybrid carbon/glass fibre composite materials, Compos. - A: Appl. Sci. Manuf. 84 (2016) 134-146.

[41] M. Hojo, M. Mizuno, T. Hobbiebrunken, T. Adachi, M. Tanaka, S.K. Ha, Effect of fiber array irregularities on microscopic interfacial normal stress states of transversely loaded UD-CFRP from viewpoint of failure initiation, Compos. Sci. Technol. 69(11-12) (2009) 1726-1734.

[42] K.K. Jin, J.H. Oh, S.K. Ha, Effect of fiber arrangement on residual thermal stress distributions in a unidirectional composite, J. Compos. Mater. 41(5) (2006) 591-611.

[43] J.H. Oh, K.K. Jin, S.K. Ha, Interfacial strain distribution of a unidirectional composite with randomly distributed fibers under transverse loading, J. Compos. Mater. 40(9) (2005) 759-778.

[44] Hexcel, Corp. https://www.hexcel.com/. (Accessed 7 October 2021).

[45] Teijin, Ltd. https://www.teijin.com/. (Accessed 7 October 2021).

[46] B. Fiedler, M. Hojo, S. Ochiai, K. Schulte, M. Ando, Failure behavior of an epoxy matrix under different kinds of static loading, Compos. Sci. Technol. 61(11) (2001) 1615-1624.

[47] Z.P. Bažant, B.H. Oh, Crack band theory for fracture of concrete, Mat. Constr. 16(3) (1983) 155-177.

[48] ABAQUS 2016 Documentation, Dassault Systèmes Simulia Corp., Providence, 2015.

[49] F. Naya, C. González, C.S. Lopes, S. Van der Veen, F. Pons, Computational micromechanics of the transverse and shear behavior of unidirectional fiber reinforced polymers including environmental effects, Compos. - A: Appl. Sci. Manuf. 92 (2017) 146-157.

[50] R. Talreja, A.M. Waas, Concepts and definitions related to mechanical behavior of fiber reinforced composite materials, Compos. Sci. Technol. 217 (2022).

[51] B.F. Sørensen, T.K. Jacobsen, Large-scale bridging in composites: R-curves and bridging laws, Compos. - A: Appl. Sci. Manuf. 29(11) (1998) 1443-1451.

[52] P.F. Becher, F. Rose, Toughening mechanisms in ceramic systems, Materials Science and Technology, Wiley Online Library2006.

[53] Z. Suo, G. Bao, B. Fan, Delamination R-curve phenomena due to damage, J. Mech. Phys. Solids 40(1) (1992) 1-16.

[54] S. Hashemi, A.J. Kinloch, J. Williams, The analysis of interlaminar fracture in uniaxial fibre-polymer composites, Proc. R. Soc. Lond. A 427(1872) (1990) 173-199.

[55] H. Tada, P.C. Paris, G.R. Irwin, The stress analysis of cracks, Handbook, Del Research Corporation 34 (1973).

[56] M. Gentz, D. Armentrout, P. Rupnowski, L. Kumosa, E. Shin, J.K. Sutter, M. Kumosa, In-plane shear testing of medium and high modulus woven graphite fiber reinforced/polyimide composites, Compos. Sci. Technol. 64(2) (2004) 203-220.

[57] J.C. Halpin, K.M. Finlayson, Primer on composite materials analysis, Routledge2017.

[58] W. Chang, L.F. Rose, M.S. Islam, S. Wu, S. Peng, F. Huang, A.J. Kinloch, C.H. Wang, Strengthening and toughening epoxy polymer at cryogenic temperature using cupric oxide nanorods, Compos. Sci. Technol. 208 (2021) 108762.

[59] M.S. Islam, L.F. Benninger, G. Pearce, C.-H. Wang, Toughening carbon fibre composites at cryogenic temperatures using low-thermal expansion nanoparticles, Compos. - A: Appl. Sci. Manuf. 150 (2021).

[60] Y. Bai, Z. Wang, L. Feng, Interface properties of carbon fiber/epoxy resin composite improved by supercritical water and oxygen in supercritical water, Mater. Des. 31(3) (2010) 1613-1616.

Figures and Tables
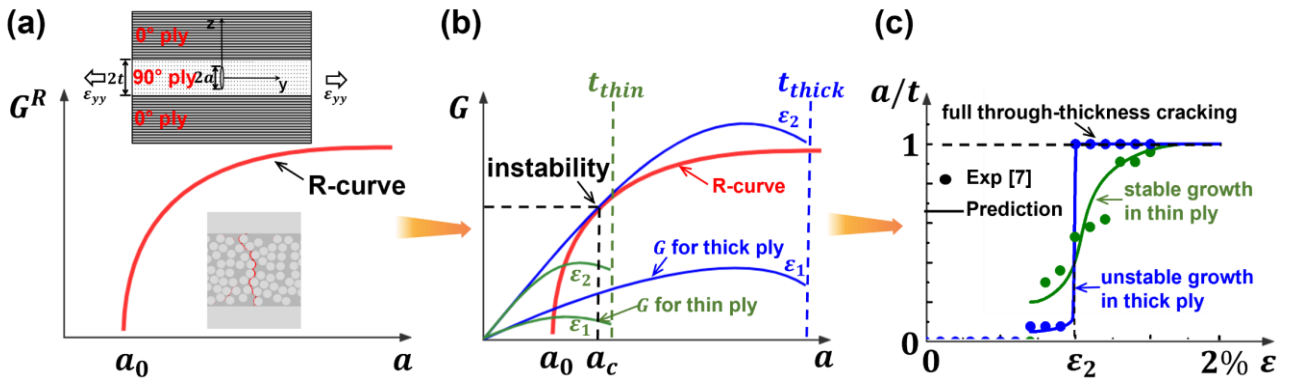
Fig. 1 Predicting the stability of crack growth. (a) A schematic R-curve (inset shows a centre crack in a 90° ply); (b) variation of the energy release rate with crack length for a thin ply (green curves) and a thick ply (blue curves), for two values of applied strain; (c) predicted crack growth behaviour.
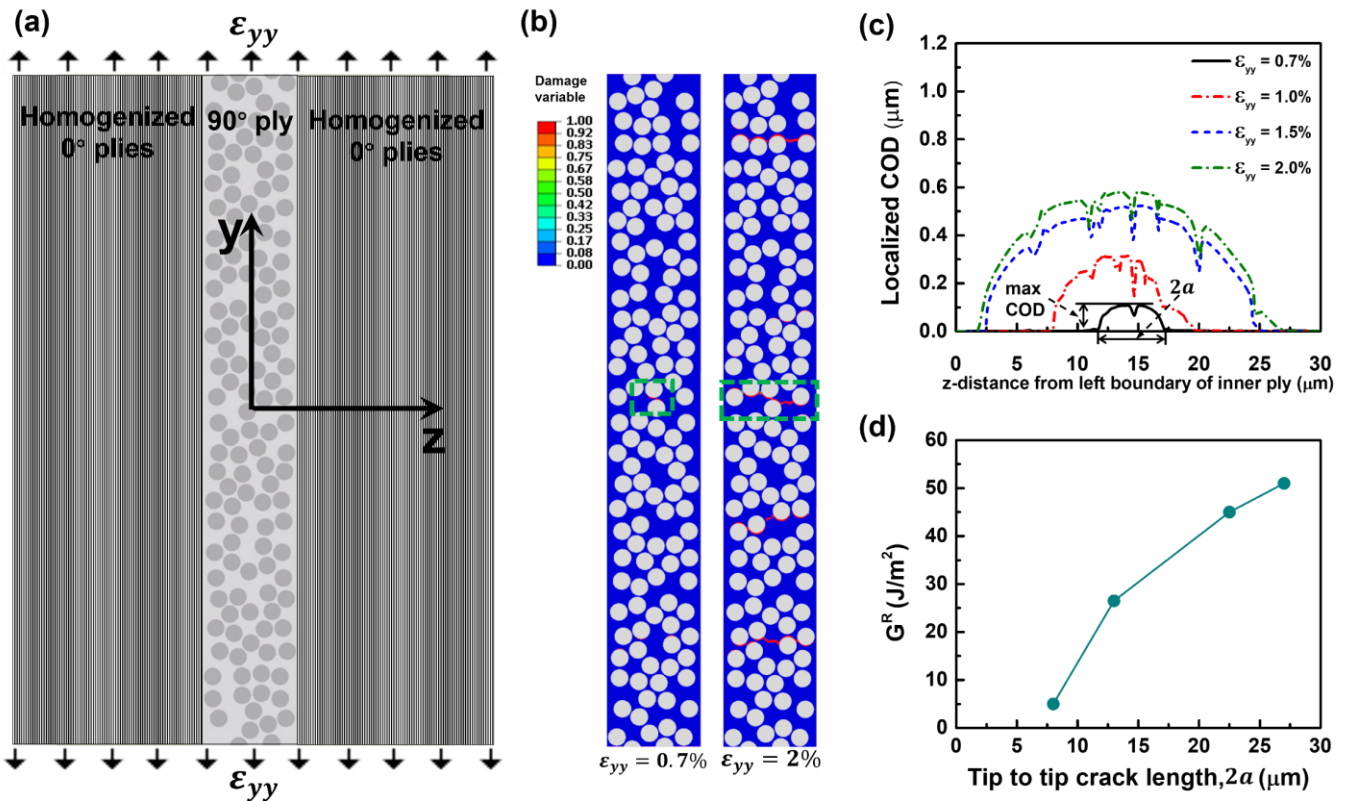
Fig. 2 Micromechanical simulation of through-thickness cracking in a crossply laminate. (a) Model geometry; (b) simulation results for two values of applied strain, with the location of failure initiation indicated by a dashed box; (c) crack opening profiles for increasing applied strain; (d) crack growth resistance as estimated from (c).

654
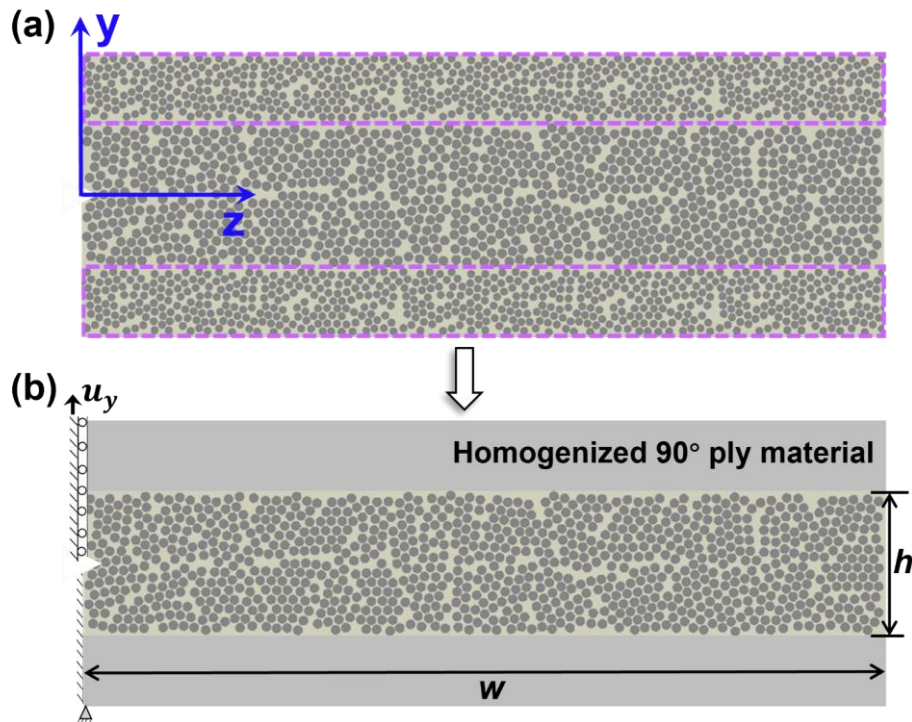
Fig. 3 Micromechanical simulation of the R-curve. (a) Cross-sectional view of 90° ply showing the coordinate

axes; (b) detailed micromechanical modelling only within an embedded cell, for computational efficiency.

657
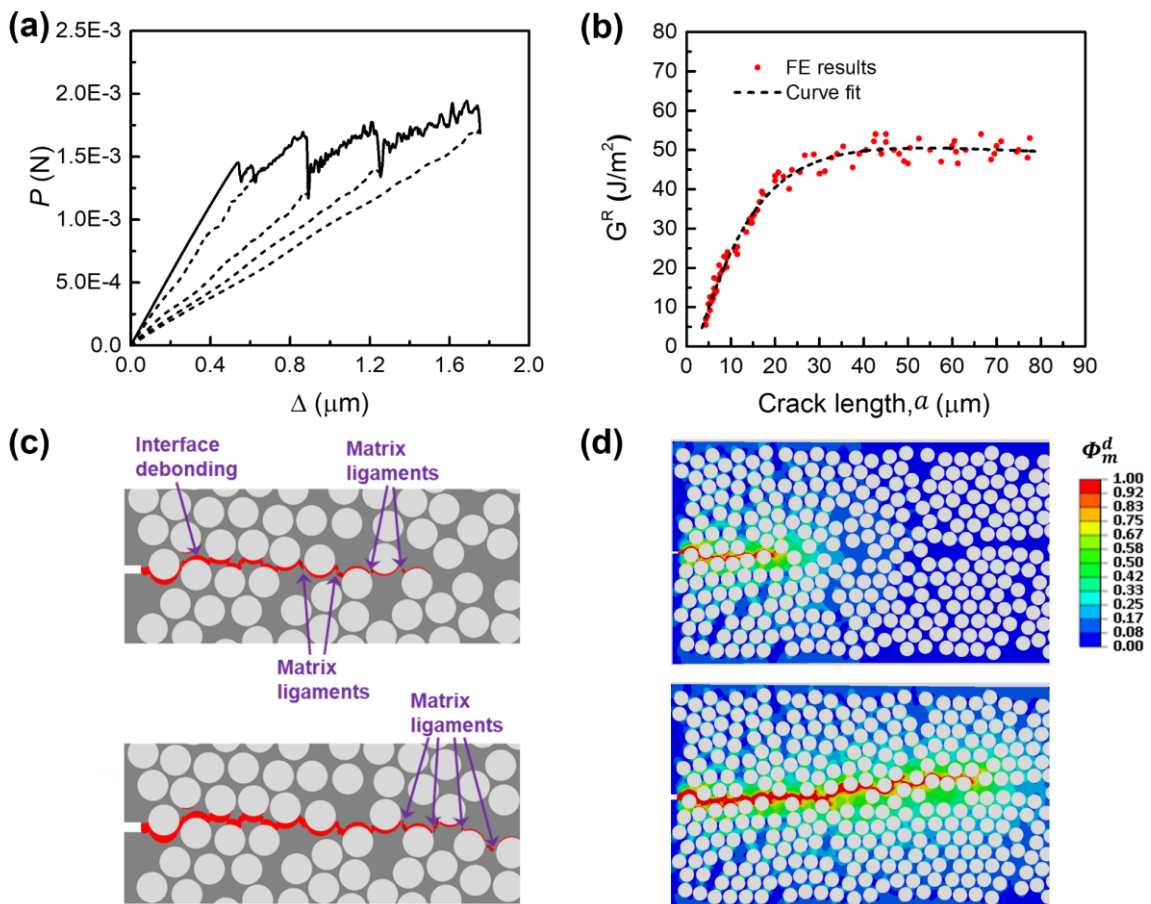
Fig. 4 The R-curve. (a) A representative load-displacement plot; (b) R-curve derived from the simulation results;

(c) crack path showing bridging by unbroken ligaments behind the advancing crack tip; (d) contour map of the

damage activation variable showing that damage zone is well contained within the embedded cell.
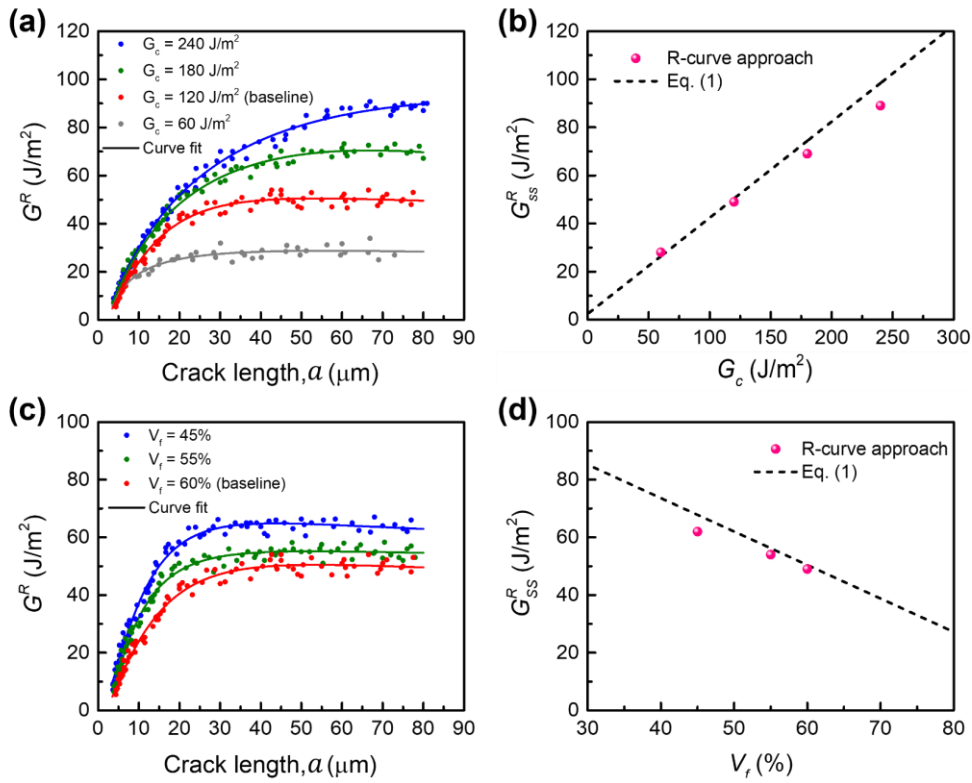
Fig. 5 Parametric variations of the R-curve. (a) R-curves for various values of matrix toughness; (b) linear variation of the steady-state resistance G_{ss}^R versus matrix toughness, compared with a rule-of-mixtures estimate (dashed line); R-curves for various values of fibre volume fraction; (d) linear variation of G_{ss}^R, compared with rule-of-mixtures estimate (dashed line).
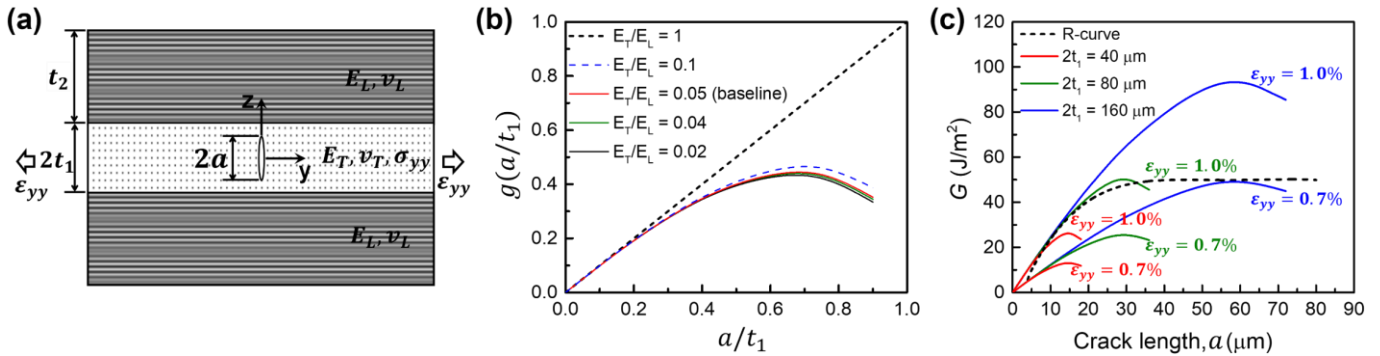
Fig. 6 Energy release rate for through-thickness cracking. (a) Model geometry and applied load; (b) normalised energy release rate vs crack length for various ply thicknesses, and two values of applied strain.
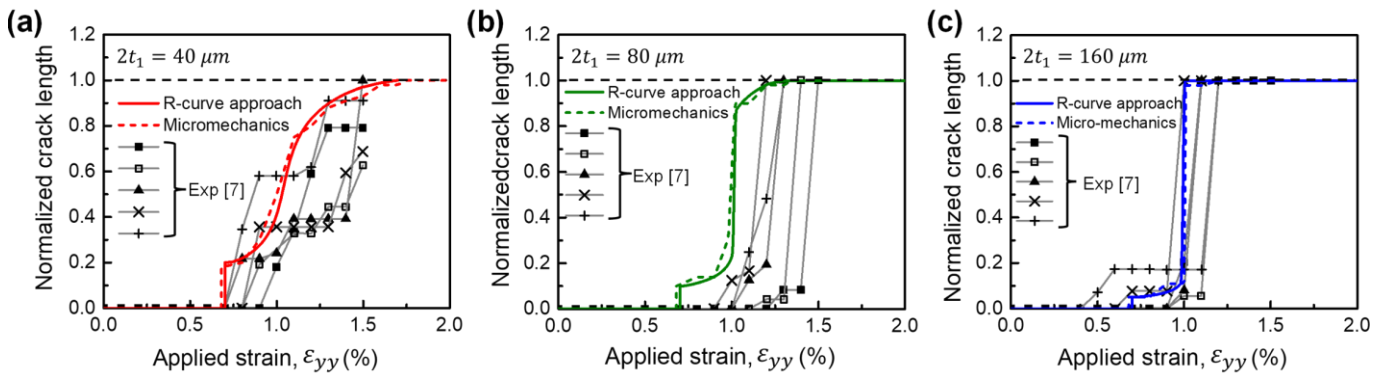
Fig. 7 Predicted crack growth behaviour based on R-curve (continuous curves), compared with the experimental observations in [7], shown as data points, and micromechanical simulation results (dashed curves). (a) Inner layer thickness $2t_1 = 40$ µm; (b) $2t_1 = 80$ µm; (c) $2t_1 = 160$ µm.

22

673

Fig. 8 R-curves in the presence of intra-ply thermal residual stress. (a) Increased crack growth resistance relative

to simulations without residual stress; (b) linear variation of steady-state resistance G_{ss}^R versus matrix toughness;

the arrow indicates the predicted change in G_{ss}^R if the matrix toughness is changed from its RT value to its LH2

value.

678
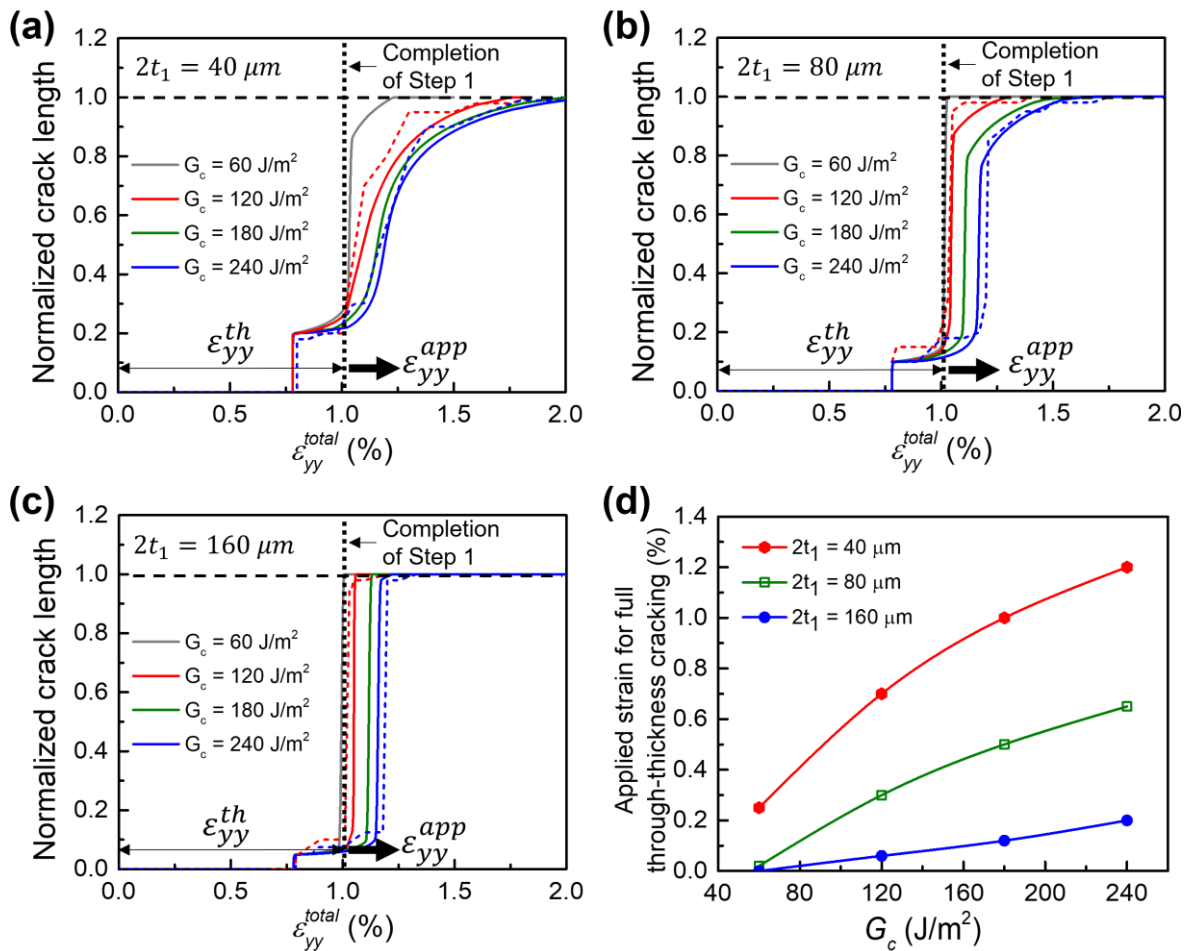
Fig. 9 Predicted crack growth behaviour as a function of total strain (i.e. thermal and applied strain), for various

ply thicknesses. (a) Inner layer thickness $2t_1 = 40$ µm; (b) $2t_1 = 80$ µm; (c) $2t_1 = 160$ µm; (d) applied strain for

full through-thickness cracking versus matrix toughness.
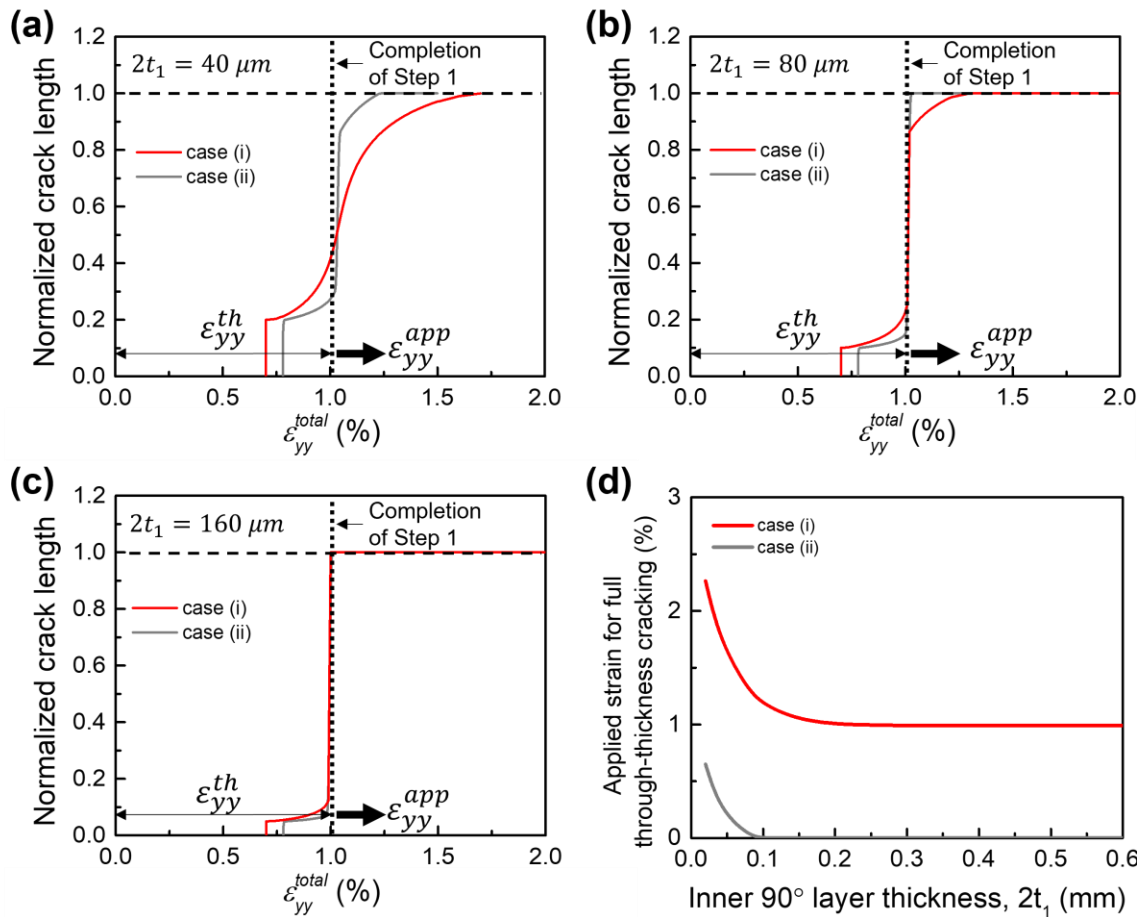
Fig. 10 Predicted crack growth behaviour considering a reduction in matrix toughness at low temperature. (a) Inner layer thickness $2t_1 = 40\ \mu m$; (b) $2t_1 = 80\ \mu m$; (c) $2t_1 = 160\ \mu m$; (d) applied strain for full through-thickness cracking versus 90°-layer thickness.
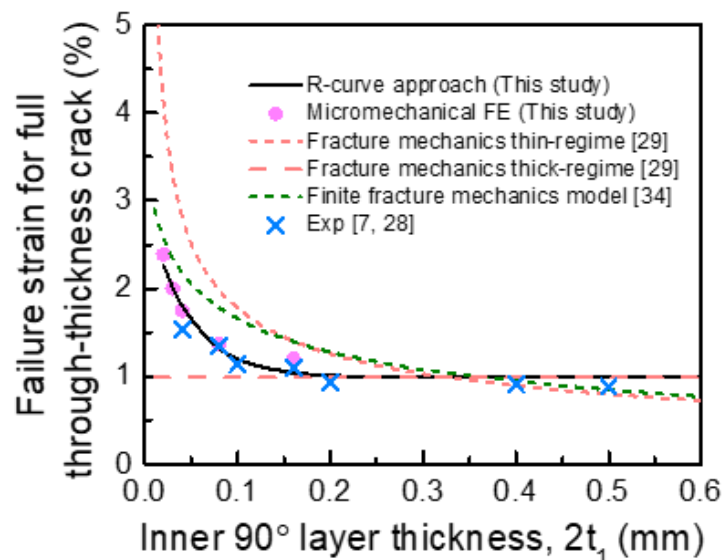
Fig. 11 Comparison of ply failure strain for full through-thickness cracking based on the present R-curve approach with experimental observations and with currently available theoretical models for ply cracking. (Note: readers are referred to [29, 34] for the implementation of both analytical models. The constant $G_{mc} = 220\ J/m^2$ as originally used in [29, 34] is retained here, and no thermal residual stress is considered for simplicity.)

Table 1

Carbon fibre material properties

Young's moduli		Poisson's ratio	Shear moduli		Coefficient of thermal expansion		Density
E_L (MPa)	E_T (MPa)	v_L	G_L (MPa)	G_T (MPa)	α_L (K^{-1})	α_T (K^{-1})	ρ (kg/mm^3)
279000	15000	0.2	15000	7000	-0.7×10^{-6}	12×10^{-6}	1.79×10^{-9}

692 Note: the subscript L and T denote the longitudinal and transverse, respectively.

Table 2

Epoxy matrix material properties

Material property	Value	Ref.
Young's modulus E (MPa)	3760	[14]
Poisson's ratio v	0.39	[46]
Plastic Poisson's ratio v_p	0.3	[8]
Fracture toughness G_c (J/m^2)	120	[58]
Tensile strength X_m^t (MPa)	93	[46]
Compressive strength X_m^c (MPa)	410	[46]
Coefficient of thermal expansion α (K^{-1})	55×10^{-6}	[58]
Density ρ (kg/mm^3)	1.3×10^{-9}	[8]

693

Table 3

Fibre–matrix interface properties

Initial stiffness	Interface strengths [60]		Interface fracture energy [20]		B-K law parameter [8]
K (MPa/mm)	t_1^0 (MPa)	t_2^0, t_3^0 (MPa)	G_{Ic}^{int} (J/mm^2)	$G_{IIc}^{int}, G_{IIIc}^{int}$ (J/mm^2)	η
10^8	80	53	4	8	1.45

694

Table 4

Homogenized composite properties

E_L (MPa)	E_T (MPa)	v_L	G_L (MPa)	G_T (MPa)	α_L (K^{-1})	α_T (K^{-1})	ρ (kg/mm^3)
168800	8796	0.3	4078	3180	-0.12×10^{-6}	37.5×10^{-6}	1.59×10^{-9}

695

Supplementary Material for:

Through-thickness crack growth resistance in fibre composites and its role in preventing ply

cracking in cross-ply laminates

Wenkai Chang[a], L. R. Francis Rose[b], Shuying Wu[a, c], Anthony J. Kinloch[d], Chun H. Wang[a*]

[a] School of Mechanical and Manufacturing Engineering, University of New South Wales, Sydney, NSW 2052, Australia.

[b] Defence Science and Technology Group, Melbourne, VIC 3207, Australia.

[c] School of Engineering, Macquarie University, Sydney, NSW 2109, Australia.

[d] Department of Mechanical Engineering, Imperial College London, South Kensington Campus, London SW7 2AZ, U.K.

*Corresponding author: Chun-Hui Wang (E-mail: chun.h.wang@unsw.edu.au Tel: +61 2 93853232)

S1. Constitutive modelling of epoxy phase

The epoxy matrix is modelled using an isotropic elastic-plastic with damage constitutive model proposed by Melro et al. [1]. In the present work, the epoxy model described in [1-5] is implemented as a VUMAT user subroutine in Abaqus [6]. The initial elastic behaviour is defined by a linear relation between the stress tensor and the elastic strain. Then, to appropriately capture the inelastic behaviour of epoxy polymers [7, 8] and the hydrostatic pressure dependency [8], this constitutive model is based on the paraboloidal yield and failure criteria, and uses a thermodynamically consistent damage model to predict damage growth. The paraboloidal yield criterion is defined as [1, 9]:

$$f(\sigma, \sigma_c, \sigma_t) = 6J_2 + 2I_1(\sigma_c - \sigma_t) - 2\sigma_c\sigma_t, \tag{S1}$$

where σ is Cauchy stress tensor, J_2 is the second invariant of deviatoric stress tensor, I_1 is the first invariant of the stress tensor and σ_c and σ_t denote the tensile and compressive yielding stresses, respectively. A non-associative flow rule [1] is also introduced to correct the volumetric deformation

26   in plastic regime. The tensile and compressive hardening laws are defined as two piecewise functions

27   of the equivalent plastic strain. The hardening data of both tension and compression yield curves has

28   been extracted from the experimental results in [8], which characterizes the stress-strain behaviour of

29   a very typical Bisphenol-A type plain epoxy resin (i.e., Toho # 113) [8]. The damage onset of the

30   epoxy matrix is defined by a damage activation function [1]:

31    $F_m^d = \Phi_m^d - r_m = 0,$ (S2)

32   where r_m is an internal variable related with the damage variable d_m, while the damage activation

33   variable, Φ_m^d, is defined as [1]:

34    $\Phi_m^d = \dfrac{3\tilde{J}_2 + \tilde{I}_1(X_m^c - X_m^t)}{X_m^c X_m^t}.$ (S3)

35   The invariants $\tilde{J}_2$ and $\tilde{I}_1$ are determined using the effective stress tensor as defined in [1], while X_m^c

36   and X_m^t denote the ultimate compressive and tensile strengths. The internal variable r_m is defined as

37   [1]:

38    $r_m = max\left\{1, \max_{t \to \infty}\{\Phi_{m,t}^d\}\right\}.$ (S4)

39   The relationship between r_m and d_m is given by an exponential damage evolution law [1, 5] which

40   is implemented along with the Bažant's crack band model [10] to mitigate the mesh size dependency

41   due to the material softening:

42    $d_m = 1 - \dfrac{e^{A_m\left(3 - \sqrt{7 + 2r_m^2}\right)}}{\sqrt{7 + 2r_m^2} - 2},$ (S5)

43   where A_m is the parameter determined by conducting the regularization of the computed energy

44   dissipation of elements [1]. This involves using the fracture energy of the epoxy matrix, G_{mc} and the

45   characteristic element size, l^e, according to the Bažant's crack band model [10]. From the above

46   definition of the damage model (i.e., Eqs. (S3-5)), it is noteworthy that (i) when the epoxy matrix is

47   in an undamaged condition, $0 \le \Phi_m^d < 1$ and $r_m = 1$, leading to $d_m = 0$; (ii) when the damage

2

48   criterion has been activated, $\Phi_m^d \geq 1$ and $r_m = \Phi_m^d$, leading to $0 \leq d_m \leq 1$; (iii) $d_m = 1$

49   corresponds to when the material is fully damaged. More details about the computational

50   implementation of the constitutive model are presented in [1, 5]. The stress-strain response of the

51   epoxy model is schematically illustrated in Fig. S1 and the relevant material properties are listed in

52   Table 2 of the main paper.
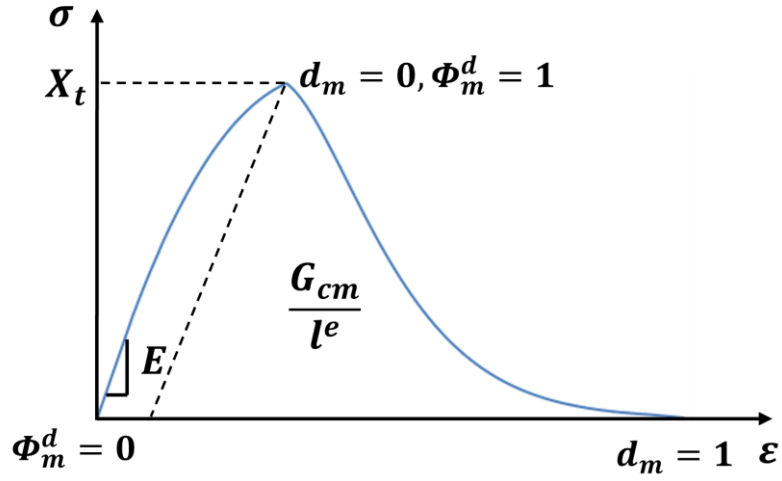
53

54   **Fig. S1** Schematic of the stress-strain response of the epoxy matrix.

55

S2. Verification of the epoxy model
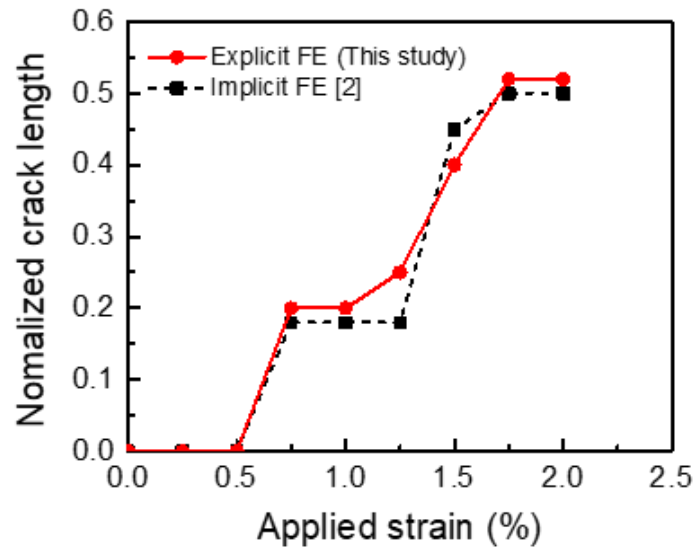
Fig. S2 Comparison between the present explicit approach and the implicit implementation in [4], with respect to the normalized crack length in an inner $90°$ layer of thickness $20 \ \mu m$ and outer layers of thickness $75 \ \mu m$.

S3. Interlaminar properties

Table S1
Interlaminar properties for the interfaces between inner and outer layers [4]

Initial stiffness	Interface strengths		Interface fracture energy		B-K law parameter
K (MPa/mm)	t_0^n (MPa)	t_0^s (MPa)	G_{int}^n (J/mm^2)	G_{int}^s (J/mm^2)	η
10^8	93	71	0.277	0.788	1.634

S4. Estimation of the crack-growth resistance from the crack opening profiles

The crack-growth resistance G^R, based on the tip-to-tip crack length $2a$ of the through-thickness matrix crack and the maximum COD δ_{max} for various levels of strain, as indicated by the crack opening profiles in Fig. 2(c) of the main paper, is calculated by the following formula:

$$G^R = \frac{\pi E_T}{16(1 - v_T^2)} A^2 a,$$

$$A = \frac{\delta_{max}}{a}, \tag{S6}$$

where $E_T = 8796\ MPa$ and $v_T = 0.32$, denoting the transverse elastic modulus and Poisson's ratio of the uncracked lamina in the present study.

S5. Initial attempt on generating the R-curve using two neighbouring loading fibres
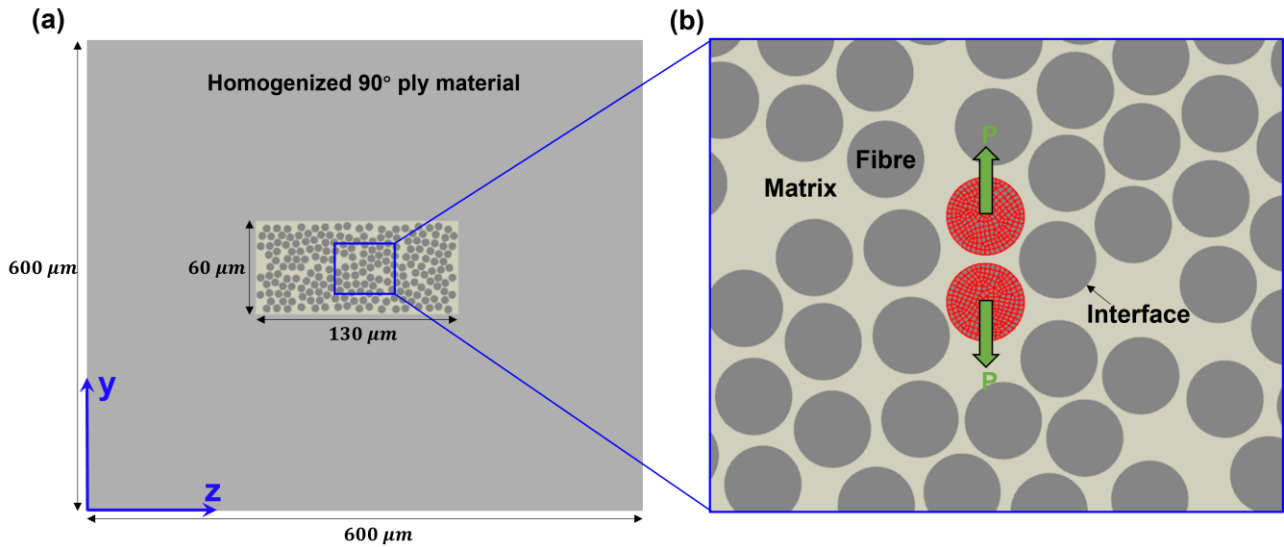
Fig. S3 Configuration of the model for initial attempt on generating the R-curve using two neighbouring loading fibres.

As mentioned in Section 3 of the main paper, the finite element (FE) model for the initial attempt on generating the R-curve computationally is shown by Fig. S3(a). The entire model consists of 90° ply material only. For computational efficiency, a rectangular micromechanical model is

5

82   embedded within a square region. The same material properties, mesh size and element types as

83   described in Section 3 of the main paper are employed for both the homogenized (elastic) region and

84   the micromechanical model region. The displacement field is assumed to be continuous across the

85   interfaces between the embedded cell and the homogenized outer portions. The model thickness in

86   the x-direction (the fibre axis) is twice the average element size within the embedded cell, and periodic

87   boundary conditions are applied to the faces normal to the x-axis.

88   There is no pre-existing crack in this model. To initiate the matrix cracking in a natural manner

89   at the fibre-matrix interface and thus to generate the R-curve with the progression of the matrix crack,

90   two neighbouring fibres, with a relatively small inter-fibre spacing, which are aligned with the y-axis

91   direction are chosen to be the load application points as shown in Fig. S3(b). All nodes of the upper

92   loading fibre are given a specified vertical displacement u_y, whereas all nodes of the lower loading

93   fibres are held fixed. The resulting nodal forces for the upper loading fibres are summed to obtain the

94   force P, whereas the displacement is given by $\Delta = u_y$.

95
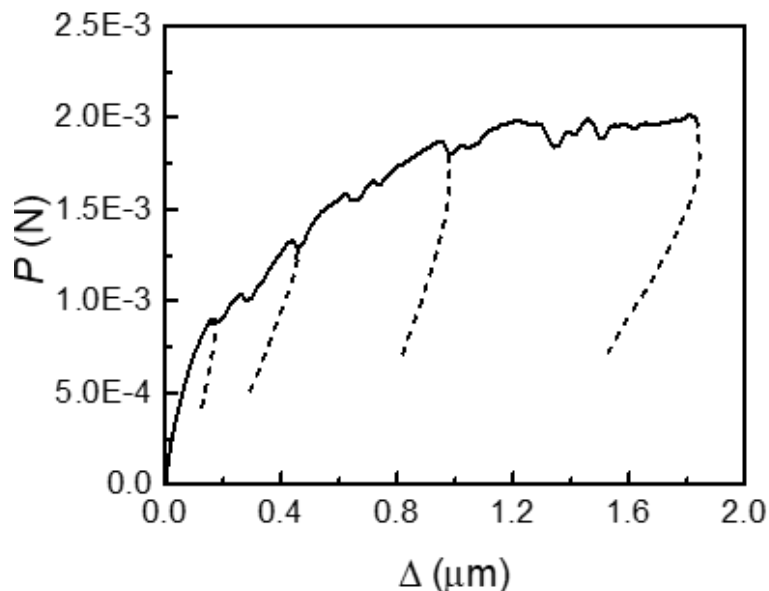
96

97   **Fig. S4** The load-displacement plot.

98

6

99　　　　　The load-displacement $(P - \Delta)$ curve obtained in this manner is shown in Fig. S4. This curve

100　　　includes some periodical unloading curves that do not extrapolate back to the origin, indicating that

101　　　model response is not linearly elastic. The contour plot of damage variable in Fig. S5(a) shows that

102　　　the microcracking does indeed initiate at the fibre-matrix interface (i.e. debonding) with the tip-to-tip

103　　　length of the matrix crack $2a$ indicated by the green arrow, which is in accord with the previous

104　　　experimental and computational observations [4, 11, 12] as well as the present micromechanical

105　　　simulation results in Fig. 2(b) of the main paper. With continuing to apply the load, however, some

106　　　matrix damages appear in the direction of loading, as indicated by the yellow dashed box in Fig S5(b),

107　　　which are not directly associated with the main crack growth process that is transverse to the loading

108　　　direction. These damages are mainly caused by the compressive and shear deformation of the matrix

109　　　near the fibres, due to the squashing effect caused by the upper and lower loading fibres, which does

110　　　not conform to the intended application of the R-curve for the context of interest. Furthermore, Fig.

111　　　S6 shows the plastic zone generated by this approach of loading. It is now clear that the severe non-

112　　　associated plastic deformation and damage caused by the loading fibres along the direction of loading

113　　　are responsible for the inelastic unloading response shown in Fig. S4, and the contribution of this

114　　　extraneous energy dissipation to the work of fracture could not readily be quantified.
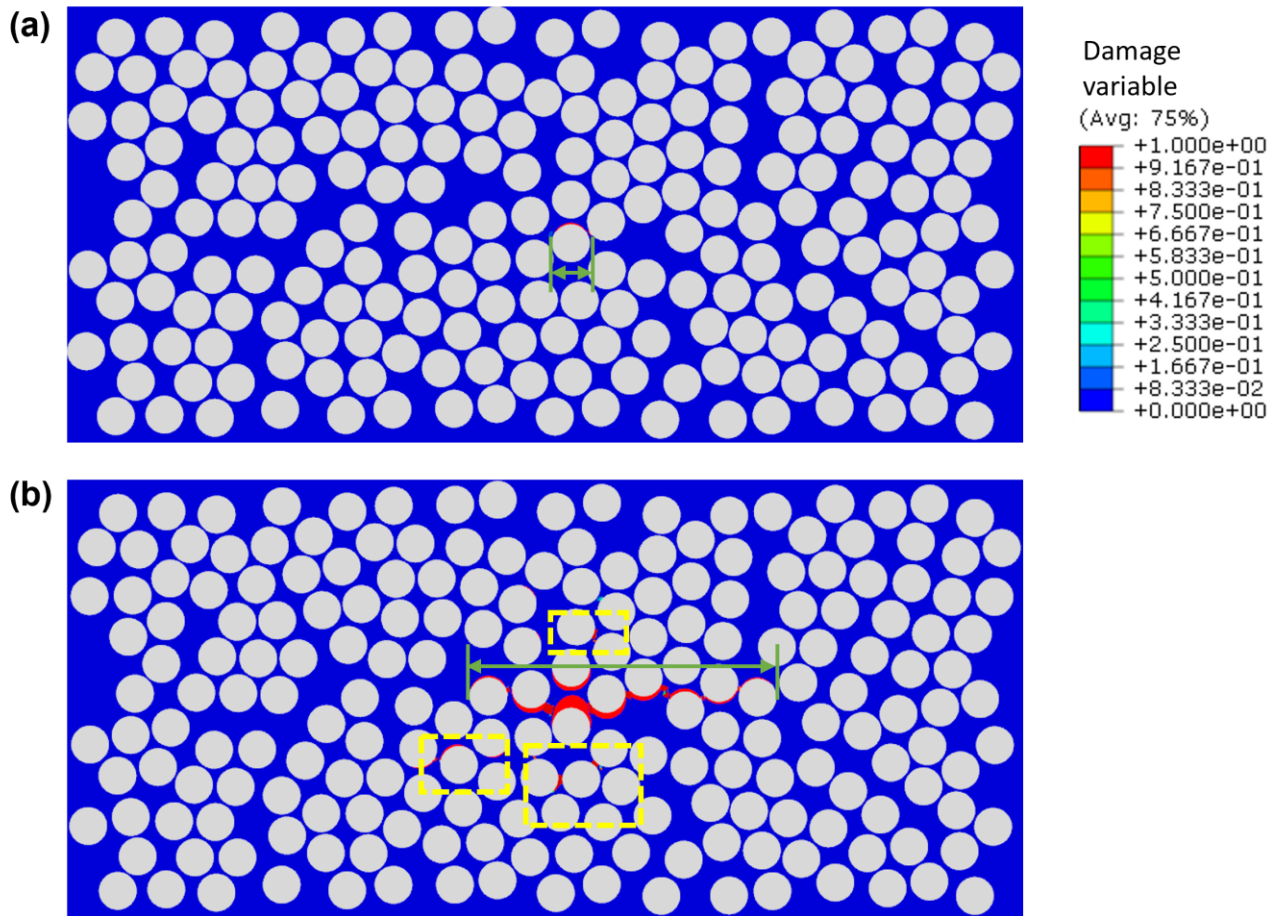
Fig. S5 Contour maps of the damage variable at the tip-to-tip length of the matrix crack of (a) 5 μm and of (b) 40 μm.
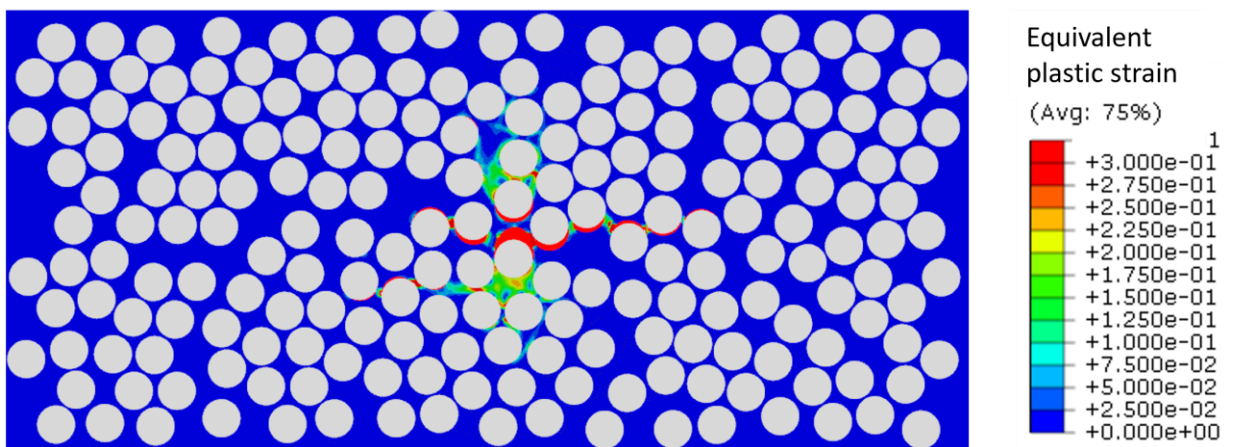
Fig. S6 Contour maps of the equivalent plastic strain at the tip-to-tip length of the matrix crack of 40 μm.

8

122 **S6. Curve fit of the results for $g(a/t_1)$, for $E_T/E_L = 0.05$**

123

Linear model Poly4:
  f(x) = p1*x^4 + p2*x^3 + p3*x^2 + p4*x + p5
Coefficients (with 95% confidence bounds):
  p1 =   -0.3634 (-0.9178, 0.191)
  p2 =   -0.1238 (-1.135, 0.887)
  p3 =   -0.3013 (-0.8864, 0.2837)
  p4 =   1.028 (0.9139, 1.142)
  p5 = -0.0003371 (-0.006064, 0.00539)

Goodness of fit:
SSE: 3.723e-06
R-square: 1
Adjusted R-square: 0.9999
RMSE: 0.001364
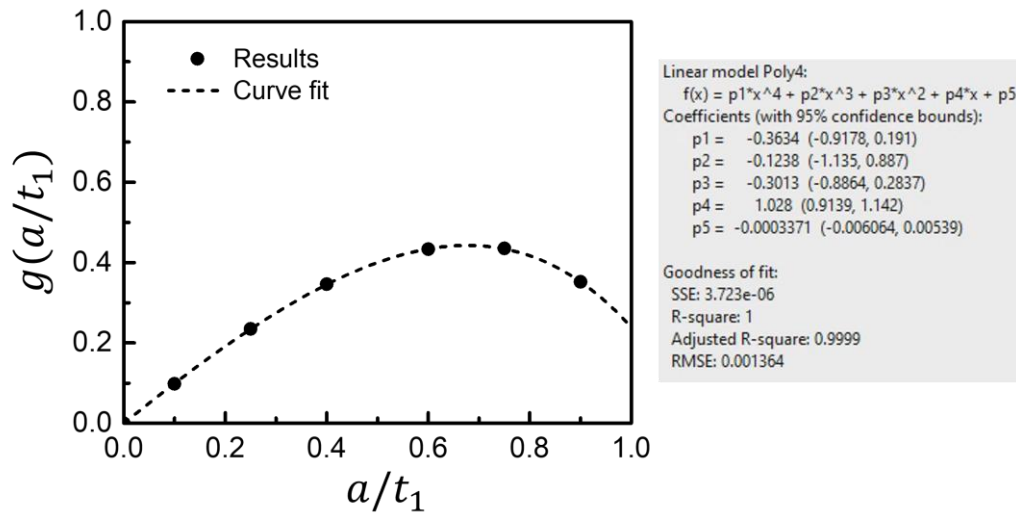
124

125 **Fig. S7** Fourth-order polynomial curve fit of the results for $g(a/t_1)$ in a/t_1, for $E_T/E_L = 0.05$, along

126 with the curve-fit quality analysis done by using MATLAB [13].

127

S7. Intra-ply thermal residual stresses at the completion of Step 1

(a) End of Step 1:

(b)

(c) $a = 76\ \mu m$ in Step 2:

129
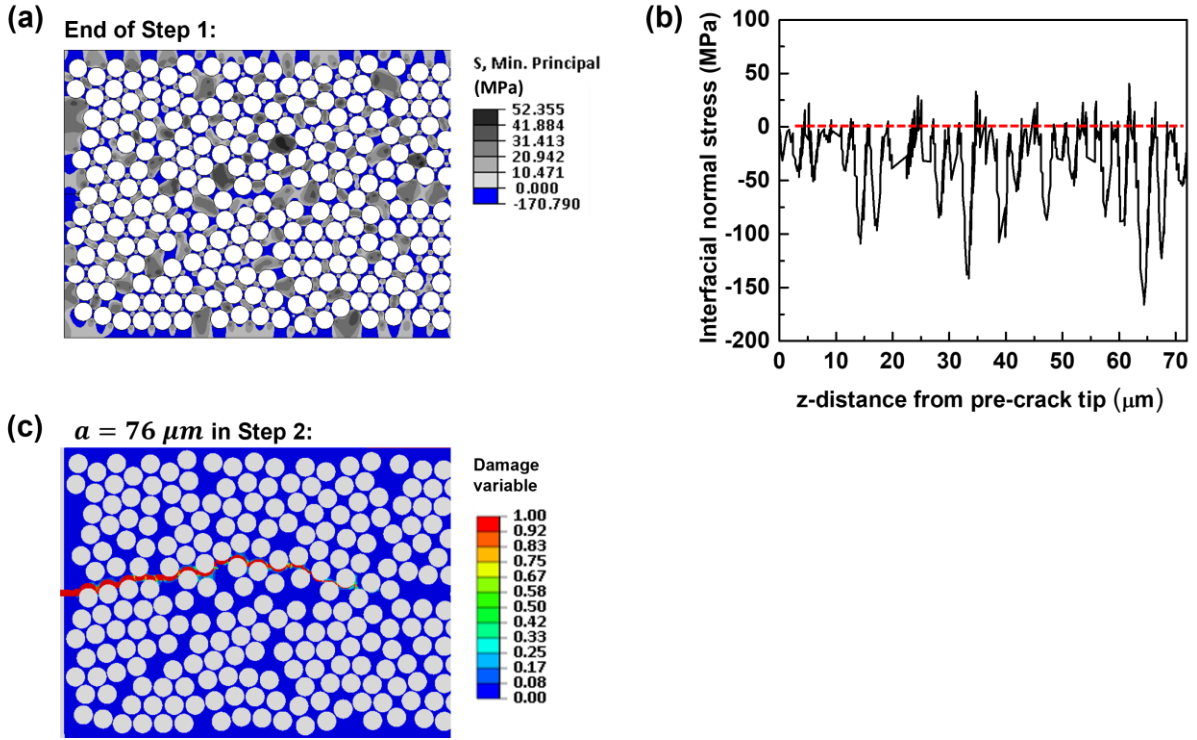
Fig. S8 (a) The intra-ply thermal residual stresses field at the completion of Step 1. (b) The interfacial normal stress at the completion of Step 1, along the prospective crack path as (c) the crack of length of 76 μm generated in Step 2.

S8. Laminate analysis for calculating the thermal residual strain at the ply level, ε_{yy}^{th}

Consider the cross-ply laminate shown in Fig. 6(a) of the main paper, which has undergone a quenching process (Step 1) with a resulting temperature change $\Delta T = -278K$ as given in Section 5.1 of the main paper, the thermal strains in a ply are [14]:

$$\{\varepsilon\}_{12}^{T} = [\theta]^{-T}\{\alpha_L\}\Delta T - \{\alpha_P\}\Delta T, \tag{S7}$$

where the subscripts "12" denote quantities in the local material coordinate (i.e. fibre direction=1, lateral direction=2), α the coefficient of thermal expansion (CTE). The subscripts "P" and "L" signify quantifies pertinent to the ply and laminate, and $[\theta]^{-T}$ the transfer matrix given by:

142

10

143 $$[\theta]^{-T} = \begin{bmatrix} m^2 & n^2 & mn \\ n^2 & m^2 & -mn \\ -2mn & 2mn & m^2 - n^2 \end{bmatrix},$$

144 $m = \cos(\theta), n = \sin(\theta).$ (S8)

145 For the inner 90° ply, $\theta = 90°$. Having known the material properties of a ply including CTEs $\{\alpha_L\}$

146 (see Table 4 of the main paper), the laminate CTEs $\{\alpha_P\}$ can be calculated by using conventional

147 lamination theory [15]. Finally, the lateral thermal residual strain ε_{yy}^{th} incorporated in Eq. (4) of the

148 main paper is:

149 $\varepsilon_{yy}^{th} = \varepsilon_{22}^{T},$ (S9)

150 where ε_{22}^{T} is the component of $\{\varepsilon\}_{12}^{T}$ pertinent to the lateral strain.

151 In Figs. 9(a-c) and Figs. 10(a-c) of the main paper, the dotted vertical lines represent the

152 thermal strain on 90° layer ε_{yy}^{th} at the completion of Step 1. There is little change in the value of ε_{yy}^{th}

153 for various inner layer thickness: $\varepsilon_{th} = 1.04\%$ for $2t_1 = 40\ \mu m$, and $\varepsilon_{th} = 1.03\%$ for $2t_1 =$

154 $160\ \mu m$. This lack of sensitivity to the inner layer thickness is partly the consequence due to the

155 relatively thick outer layer thickness employed in the present laminate configuration to conform to

156 the experimental setup by Saito et al. [11]. Nevertheless, these values of inter-ply residual strain

157 exceed the failure-initiation strain for fibre-matrix debonding, particularly when $2t_1 = 160\ \mu m$ for

158 which even the full-thickness cracking is predicted to occur when $G_c = 60\ J/m^2$, i.e., no applied

159 strain is required to cause ply cracking, as can be seen from Fig 9(d) of the main paper. The

160 representative contours illustrating the extent of matrix cracking for baseline matrix toughness $G_c =$

161 $120\ J/m^2$ at the completion of Step 1 of the micromechanical simulations are presented below in Fig.

162 S9.

163
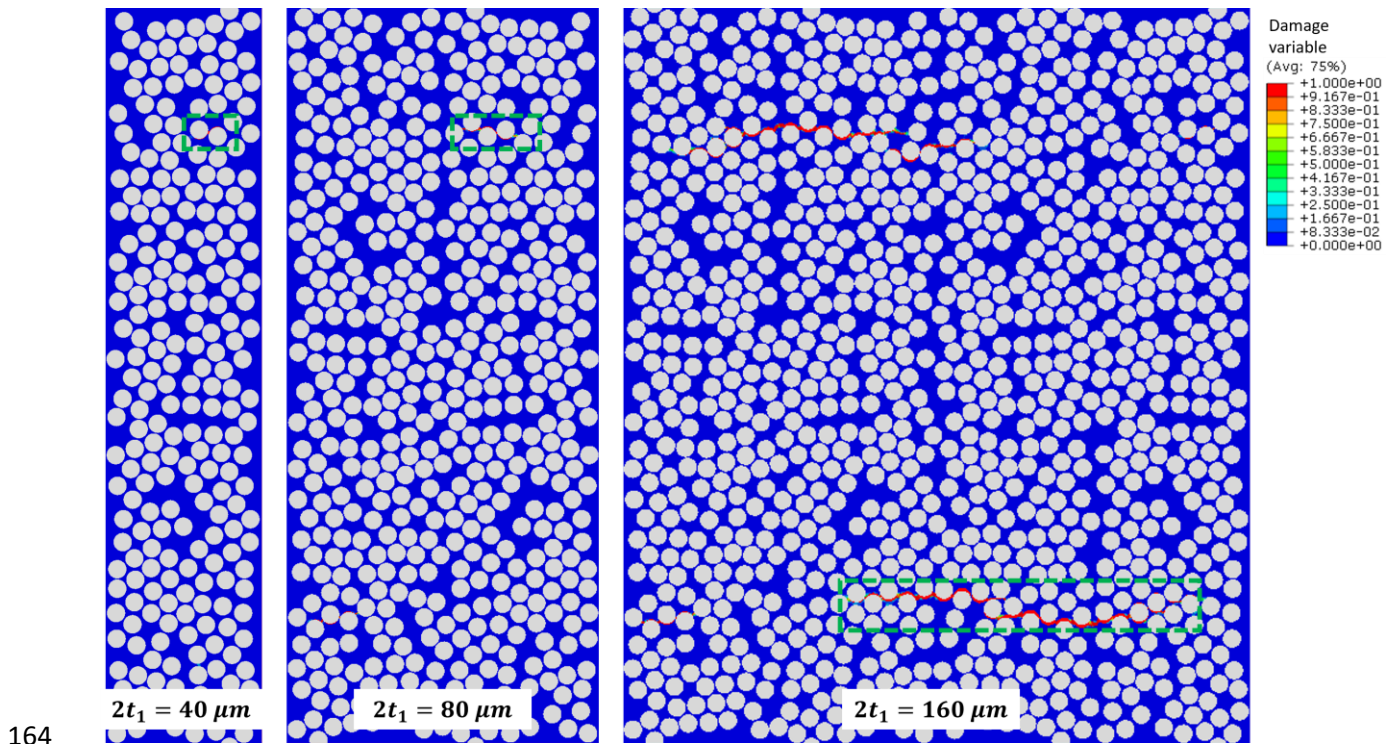
Fig. S9 Contour maps of the damage variable at the completion of Step 1 for various inner 90° layer thicknesses: $2t_1 = 40, 80$ and $160 \; \mu m$ (the through-thickness cracks that are selected for measuring the crack length are indicated by the green dashed rectangles, and only the inner 90° layer is shown).

References

[1] A.R. Melro, P.P. Camanho, F.M. Andrade Pires, S.T. Pinho, Micromechanical analysis of polymer composites reinforced by unidirectional fibres: Part I – Constitutive modelling, Int. J. Solids Struct. 50(11-12) (2013) 1897-1905.

[2] A. Arteiro, G. Catalanotti, A.R. Melro, P. Linde, P.P. Camanho, Micro-mechanical analysis of the effect of ply thickness on the transverse compressive strength of polymer composites, Compos. - A: Appl. Sci. Manuf. 79 (2015) 127-137.

[3] A. Arteiro, G. Catalanotti, J. Reinoso, P. Linde, P.P. Camanho, Simulation of the mechanical response of thin-ply composites: from computational micro-mechanics to structural analysis, Arch. Comput. Methods Eng. 26(5) (2018) 1445-1487.

179   [4] A. Arteiro, G. Catalanotti, A.R. Melro, P. Linde, P.P. Camanho, Micro-mechanical analysis of the

180   in situ effect in polymer composite laminates, Compos. Struct. 116 (2014) 827-840.

181   [5] Q. Sun, Z. Meng, G. Zhou, S.-P. Lin, H. Kang, S. Keten, H. Guo, X. Su, Multi-scale computational

182   analysis of unidirectional carbon fiber reinforced polymer composites under various loading

183   conditions, Compos. Struct. 196 (2018) 30-43.

184   [6] ABAQUS 2016 Documentation, Dassault Systèmes Simulia Corp., Providence, 2015.

185   [7] W. Chang, L.F. Rose, M.S. Islam, S. Wu, S. Peng, F. Huang, A.J. Kinloch, C.H. Wang,

186   Strengthening and toughening epoxy polymer at cryogenic temperature using cupric oxide nanorods,

187   Compos. Sci. Technol. 208 (2021) 108762.

188   [8] B. Fiedler, M. Hojo, S. Ochiai, K. Schulte, M. Ando, Failure behavior of an epoxy matrix under

189   different kinds of static loading, Compos. Sci. Technol. 61(11) (2001) 1615-1624.

190   [9] Z. Ullah, L. Kaczmarczyk, C.J. Pearce, Three-dimensional nonlinear micro/meso-mechanical

191   response of the fibre-reinforced polymer composites, Compos. Struct. 161 (2017) 204-214.

192   [10] Z.P. Bažant, B.H. Oh, Crack band theory for fracture of concrete, Mat. Constr. 16(3) (1983) 155-

193   177.

194   [11] H. Saito, H. Takeuchi, I. Kimpara, Experimental evaluation of the damage growth restraining in

195   90° layer of thin-ply CFRP cross-ply laminates, Adv. Compos. Mater. 21(1) (2012) 57-66.

196   [12] R. Talreja, A.M. Waas, Concepts and definitions related to mechanical behavior of fiber

197   reinforced composite materials, Compos. Sci. Technol. 217 (2022).

198   [13] MATLAB, 9.7.0.1190202 (R2019b), The MathWorks Inc., Natick, Massachusetts, 2018.

199   [14] C.H. Wang, A multi-scale progressive damage model for laminates, Aust. J. Mech. Eng. 3(1)

200   (2006) 73-78.

201   [15] J.C. Halpin, K.M. Finlayson, Primer on composite materials analysis, Routledge2017.

202